

THESIS FOR THE DEGREE OF DOCTOR OF PHILOSOPHY  
IN SOLID AND STRUCTURAL MECHANICS

# Geometric Modeling of Thoracic Aortic Surface Morphology

Implications for Pathophysiology and Clinical Interventions

JOHAN BONDESSON

Department of Mechanics and Maritime Sciences  
Division of Dynamics  
CHALMERS UNIVERSITY OF TECHNOLOGY  
Gothenburg, Sweden 2021

Geometric Modeling of Thoracic Aortic Surface Morphology  
Implications for Pathophysiology and Clinical Interventions  
JOHAN BONDESSON  
ISBN 978-91-7905-472-4

© JOHAN BONDESSON, 2021

Doktorsavhandlingar vid Chalmers tekniska högskola  
Ny serie nr. 4939  
ISSN 0346-718X

Department of Mechanics and Maritime Sciences  
Division of Dynamics  
Chalmers University of Technology  
SE-412 96 Gothenburg  
Sweden  
Telephone: +46 (0)31-772 1000

Cover:

Illustration of a chiral thoracic aortic type B dissection after thoracic endovascular repair with a tubular endograft covering the intimal tear, parts of the aortic arch and descending aorta made by Dr. Ga-Young Suh.

Chalmers Digitaltryck  
Gothenburg, Sweden 2021

Geometric Modeling of Thoracic Aortic Surface Morphology  
Implications for Pathophysiology and Clinical Interventions

JOHAN BONDESSON

Department of Mechanics and Maritime Sciences

Division of Dynamics

Chalmers University of Technology

## ABSTRACT

Vascular disease risk factors such as hypertension, hyperlipidemia and old age are all results of modern-day lifestyle, and these diseases are getting more and more common. One treatment option for vascular diseases such as aneurysms and dissections is endovascular aortic repair introduced in the early 1990s. This treatment uses tubular fabric covered metallic structures (endografts) that are implanted using a minimally invasive approach and placed to serve as an artificial vessel in a damaged portion of the vasculature. To ensure that the interventions are successful, the endograft must be placed in the correct location, and designed to sustain the hostile biological, chemical, and mechanical conditions in the body for many years. This is an interaction that goes both ways, and keeping in mind that the endograft is a foreign object placed in the sensitive vascular system, it is also important that it does not disrupt the native conditions more than necessary.

This thesis presents a segmentation and quantification methodology to accurately describe the complex morphology and motion of diseased blood vessels *in vivo* through a natural and intuitive description of their luminal surfaces. After methodology validation, a series of important clinical applications are performed, all based on non-invasive imaging. Firstly, it is shown that explicit surface curvature quantification is necessary when compared to relying solely on centerline curvature and estimation methods. Secondly, it is shown that endograft malapposition severity can be predicted from preoperative geometric analysis of thoracic aortic surfaces. Thirdly, a multiaxial dynamics analysis of cardiac induced thoracic aortic surface motion shows how thoracic endovascular aortic repair affects the deformations of the different portions of the thoracic aorta. Fourthly, the helical propagation pattern of type B aortic dissection is determined, and two distinct modes of chirality are revealed, *i.e.*, achiral and right-handed chiral groups. Finally, the effects of thoracic endovascular aortic repair on helical and cross-sectional morphology of type B dissections are investigated revealing how acuity and chirality affects the alteration due to intraluminal lining with endografts. Thus, the work presented in this thesis contributes by adding knowledge about pathology and pathophysiology through better geometric description of surface conditions of diseased thoracic aortas. This gives clinicians insights to use in their treatment planning and provides more nuanced boundary conditions for endograft manufacturers. Comprehensive knowledge about diseases, better treatment planning, and better devices are all crucial in order to improve the outcomes of performed interventions and ultimately the quality of life for the treated patients.

**Keywords:** Thoracic aorta, aneurysm, type B aortic dissection, geometric modeling, stereolithographic 3D surfaces, surface curvature, TEVAR, endograft, bird-beaking, cardiac pulsatility, helical morphology, chirality





*To my family*



## PREFACE

The work presented in this thesis was performed from the fall of 2017 to the spring of 2021 at the Division of Dynamics, Department of Mechanics and Maritime Sciences, Chalmers University of Technology, and during visits to the Vascular Intervention Biomechanics & Engineering Laboratory (VIBE lab) at the Division of Vascular Surgery, Department of Surgery, Stanford University School of Medicine, California, United States of America.

## ACKNOWLEDGEMENTS

The processes of conducting the underlying research and writing this thesis have not been straightforward nor easy. Without excellent collaborators, caring mentors and supporting family and friends, I would not have made it and I want to use this page to thank you.

I want to thank Chris Cheng for not just being a challenging supervisor and a particular co-author, but also a mentor and friend who I look up to. I especially remember and value the time we spent at Stanford, all our great conference experiences, and when I visited you in Oxford. I hope we will continue to add to this list in the future.

Kelly Suh for being a caring instructor who have not only contributed to the contents of this thesis by letting me use her beautiful anatomic sketches, but also to me learning and developing. Thank you for teaching me how to teach. Visiting you in San Diego and Long Beach were both highlights for me.

I also want to thank the team at the Division of Vascular Surgery and collaborators at Stanford. Michael Dake and Jason Lee for your clinical expertise and support, and also for the invaluable experience of allowing me in the operating room to observe.

At Chalmers, I want to start off by thanking Torbjörn Lundh for introducing me to the field, our numerous fruitful whiteboard-filling brainstorming sessions, and your guidance in my development as a researcher. I want to thank Mikael Enelund for all help with the project, and in particular, aiding me to reduce the number, and to ensure the correct placement, of commas. I also want to thank all colleagues who have given advice or helped out in any way. The financial support from the Barbro Osher Endowment enabling me to visit Stanford during the fall of 2019 was much appreciated.

I want to thank Marc and Julia Zafferano for your hospitality when I've been in California. Being able to stay with you has enriched my visits and our adventures, holiday celebrations, and discussions about idioms were all icing on the cake.

Last, but not least, I want to thank my family and friends: My mom, dad, and brother for your unconditional and genuine support. Hanna, for putting up with my stupid medical questions, for overlooking my odd working hours and grumpy mood when things were tough, and for insisting on celebrating small victories. I want to thank all my friends who have been around and giving my life meaning and joy during well-deserved breaks.

You have all contributed to this, and I'm grateful to have all of you in my life.

Gothenburg, April 2021  
Johan Bondesson



## NOMENCLATURE

2D – Two-dimensional  
3D – Three-dimensional  
BA – Brachiocephalic artery  
BBA – Bird-beak angle  
BBH – Bird-beak height  
BBL – Bird-beak length  
CAD – Computer aided design  
CBM – Centerline-based method  
CDF – Cumulative distribution function  
COM – Center of mass  
CT – Computed tomography  
CTA – Computed tomography angiography  
DNA – Deoxyribonucleic acid  
LCCA – Left common carotid artery  
LSA – Left subclavian artery  
PDF – Probability density function  
PTFE – Polytetrafluoroethylene  
RMS – Root mean square  
ROI – Region of interest  
SBM – Surface-based method  
SINE – Stent induced new entry  
TEVAR – Thoracic endovascular aortic repair



# THESIS

This thesis consists of an extended summary and the following appended papers:

- Paper A** Johan Bondesson, Ga-Young Suh, Torbjörn Lundh, Jason T. Lee, Michael D. Dake, and Christopher P. Cheng. "Automated Quantification of Diseased Thoracic Aortic Longitudinal Centerline and Surface Curvatures". *Journal of Biomechanical Engineering - Transactions of the ASME*, 142(4):041007 (9 pages) (2020). DOI:10.1115/1.4045271
- Paper B** Maxfield M. Frohlich, Ga-Young Suh, Johan Bondesson, Jason T. Lee, Michael D. Dake, Matthew Leineweber, and Christopher P. Cheng. "Thoracic Aortic Geometry Correlates with Endograft Bird-beaking Severity". *Journal of Vascular Surgery*, 72(4):1196-1205 (2020). DOI:10.1016/j.jvs.2019.11.045
- Paper C** Ga-Young Suh, Johan Bondesson, Yufei D. Zhu, Jason T. Lee, Michael D. Dake, and Christopher P. Cheng. "Multiaxial Pulsatile Dynamics of The Thoracic Aorta and Impact of Thoracic Endovascular Repair". *European Journal of Radiology Open*, 8:100333 (8 pages) (2021). DOI:10.1016/j.ejro.2021.100333
- Paper D** Johan Bondesson, Ga-Young Suh, Torbjörn Lundh, Michael D. Dake, Jason T. Lee, and Christopher P. Cheng. "Quantification of True Lumen Helical Morphology in Type B Dissections". *American Journal of Physiology - Heart and Circulatory Physiology*, 320(2):H901-H911 (2021). DOI:10.1152/ajpheart.00778.2020
- Paper E** Johan Bondesson, Ga-Young Suh, Neil Marks, Michael D. Dake, Jason T. Lee, and Christopher P. Cheng. "Influence of Thoracic Endovascular Aortic Repair on True Lumen Helical Morphology for Stanford Type B Dissections". *Accepted for publication in the Journal of Vascular Surgery*

Other publications related to, but not included in, the thesis:

- Publication I** Johan Bondesson and Torbjörn Lundh. "Biomechanical modeling of thoracic aortic surfaces". Svenska Mekanikdagarna, 2019. [https://www.kth.se/polopoly\\_fs/1.913522.1561399182!/SMD\\_2019\\_Program\\_Website.pdf](https://www.kth.se/polopoly_fs/1.913522.1561399182!/SMD_2019_Program_Website.pdf)
- Publication II** Ga-Young Suh, Brant W. Ullery, Johan Bondesson, Christopher P. Cheng, and Jason T. Lee. "Dynamic geometric changes of the thoracic aorta: implications for TEVAR and branched grafts". Congress book for the European Symposium on Vascular Biomaterials, 2019. [http://www.esvb.net/uk/telecharge.php?id=/download/Fichiers/2019/book/ESVB\\_Congress\\_Book\\_2019.pdf](http://www.esvb.net/uk/telecharge.php?id=/download/Fichiers/2019/book/ESVB_Congress_Book_2019.pdf)

Summary of appended papers and work distribution:

*Paper A:* In this paper an automated segmentation algorithm and modeling framework were developed and validated on computer generated phantoms. This included automatic cross-sectional slicing of triangulated 3D surface models and subsequent description in a Lagrangian cylindrical coordinate system. After validation, the algorithms were used to quantify longitudinal surface curvature of 37 human thoracic aortas with aneurysm or dissection. The results confirmed the hypotheses that the longitudinal surface curvature is significantly different compared to the longitudinal curvature of the centerline. It was also concluded that surface curvature cannot be approximated using a straightforward estimation method, especially not in the case of diseased thoracic aortas. Preliminary results from this study were presented at the Leipzig Interventional Course (LINC) in 2018: <https://linc2018.cncptdlx.com/media/125.pdf>.

Johan Bondesson performed methods development, validation, application on patient data, and manuscript writing, supported by Ga-Young Suh, Torbjörn Lundh and Christopher P. Cheng. Jason T. Lee and Michael D. Dake treated the patients and all authors contributed in the process of proof-reading.

*Paper B:* In this paper methods for prediction of endograft malapposition based on preoperative data were developed. Analyses were then conducted on a cohort of 20 patients who had their aneurysms or type B aortic dissection treated with TEVAR. By establishing metrics for bird-beak height, the cohort could be categorized into two subgroups: ten patients with, and ten patients without, bird-beak occurrence. For the group where bird-beak configuration was observed, analyses of the preoperative pathology showed significant correlation between inner surface curvature and inner surface curvature-diameter with bird-beak height and bird-beak angle. It was also found that the product inner surface curvature-diameter was significantly higher for this group compared to the group that did not show bird-beaking postoperatively. Preliminary results from this study were presented at LINC 2018: <https://linc2018.cncptdlx.com/media/124.pdf>.

Maxfield M. Frohlich lead the project and wrote the paper in collaboration with Ga-Young Suh under supervision of Christopher P. Cheng and Matthew Leineweber. Johan Bondesson contributed to analysis and interpretation. Jason T. Lee and Michael D. Dake treated the patients and all authors contributed in the process of proof-reading.

*Paper C:* In this paper the effects of TEVAR on multiaxial deformation due to cardiac motion was studied. The methods included modeling of ten cardiac frames for the thoracic aorta of eleven patients, before and after TEVAR and a set of metrics were extracted. Based on cross-sectional data, effective diameters could be measured. Based on the centerline, arc length and longitudinal curvature were extracted. From the surfaces the inner and outer surface curvatures could be quantified. Peak-matching methods were applied to the curvature data, to compensate for longitudinal shift of local minima and maxima. Based on this, the cardiac induced arc length deformation was found to increase for the ascending aorta, but decrease for the stented aorta from pre- to post-TEVAR. The stented aorta also showed a decrease in outer surface curvature and diametric change. Hypothesised stiffening of the stented aorta was confirmed and the results indicate that



this also affects the deformation of the ascending aorta, possibly to compensate for the altered compliance of the stented aorta. Preliminary results from this study were presented at LINC 2018: <https://linc2018.cncptdlx.com/media/137.pdf>.

Ga-Young Suh was the main responsible for this project. Johan Bondesson contributed with methods development and simulation as well as manuscript writing. Jason T. Lee and Michael D. Dake treated the patients. Yufei D. Zhu performed modeling of patient data and all authors contributed in the process of proof-reading.

*Paper D:* In this paper a dual lumen cross-sectional slicing algorithm was developed, including novel definition of metrics to describe helical morphology. Two methods (based on surface and centerline data, respectively) were introduced and subsequently used to quantify helical angle, helical twist, and helical radius. After method validation and parameter tuning in a phantom study, the two methods were utilized on a patient cohort consisting of 19 thoracic aortas with type B dissection. The phantom validation study indicated high levels of accuracy compared to analytical solutions for both methods and recommendations for parameter settings were identified. The results for the patient cohort revealed distinct a bimodal distribution of helical angle suggesting that the dissection propagation favours two modes: either they stay in the inner curve of the thoracic aorta (achiral) or forms a spiral shape (exclusively right-handed chiral). Further studies are needed to fully determine the mechanisms, but it is speculated that this propagation pattern is seen due to helicity of the blood and helically arranged fibres in the vessel wall. Preliminary results from this study were presented at the Transcatheter Cardiovascular Therapeutics conference in 2019: <https://www.tctmd.com/slide/true-lumen-helicity-intype-b-dissections>.

Johan Bondesson was the main responsible for all aspects of this paper including analysis and interpretation and manuscript writing. Jason T. Lee and Michael D. Dake treated the patients and all authors contributed in the process of proof-reading.

*Paper E:* In this paper the aim was to quantify the alteration induced by thoracic endovascular aortic repair on helical (helical angle, helical twist, and helical radius) and cross-sectional (cross-sectional area, cross-sectional circumference and cross-sectional eccentricity) metrics. Surfaces of thoracic aortas of 16 patients were constructed from computed tomography angiography images prior to and after thoracic endovascular aortic repair. There was no alteration of the helical angle or helical twist metrics in general, but the distinct grouping based on chirality pre-TEVAR vanished after operation. For the whole cohort, helical radius and cross-sectional eccentricity decreased whereas cross-sectional area and circumference increased. This indicates that the lumen follows a straighter path with cross sections allowing for lower flow resistance. Two subgroup analyses revealed how different metrics are altered for groups based on level of acuity and chirality respectively. Preliminary results from this study were presented at the annual meeting of the Western Vascular Society 2020, published in the Journal of Vascular Surgery 72(3), e337-e338. [https://www.jvascsurg.org/article/S0741-5214\(20\)31559-7/pdf](https://www.jvascsurg.org/article/S0741-5214(20)31559-7/pdf).

Johan Bondesson lead the work including outlining the study, methods development, quantification, and manuscript writing. Jason T. Lee and Michael D. Dake treated the patients and Neil Marks performed modeling of patient data. All authors contributed in the process of proof-reading.



# CONTENTS

<b>Abstract</b>	<b>i</b>
<b>Preface</b>	<b>v</b>
<b>Acknowledgements</b>	<b>v</b>
<b>Nomenclature</b>	<b>vii</b>
<b>Thesis</b>	<b>ix</b>
<b>Contents</b>	<b>xiii</b>

<b>I Extended Summary</b>	<b>1</b>
---------------------------	----------

<b>1 Background</b>	<b>1</b>
1.1 Introduction . . . . .	1
1.1.1 Purpose, Aims, and Research Questions . . . . .	2
1.1.2 Limitations . . . . .	4
1.2 Anatomy, Pathology, Interventions, and Devices . . . . .	4
1.2.1 Thoracic Aortic Anatomy . . . . .	4
1.2.2 Thoracic Aortic Pathology . . . . .	5
1.2.3 Endovascular Interventions and Devices . . . . .	7
<b>2 Geometric Modeling of Aortic Surfaces</b>	<b>9</b>
2.1 Imaging and Segmentation . . . . .	9
2.2 Cross-Sectional Slicing . . . . .	9
2.2.1 Single Lumen . . . . .	9
2.2.2 Dual Lumen . . . . .	11
2.3 Lagrangian Formulation of Surfaces . . . . .	11
2.4 Quantification Domain . . . . .	13
2.4.1 Longitudinal Region of Interest . . . . .	13
2.4.2 Longitudinal Surface Paths . . . . .	14
2.5 Metrics Definition . . . . .	15
<b>3 Validation of Models and Methodology</b>	<b>18</b>
3.1 Phantom Design . . . . .	18
3.2 Error Estimation and Parameter Calibration . . . . .	19
<b>4 Explicit and Estimated Surface Curvature</b>	<b>21</b>
<b>5 Applications on Patient-Specific Aortas</b>	<b>22</b>
5.1 Explicit Quantification of Longitudinal Curvature . . . . .	22

5.2	Endograft Malapposition Prediction . . . . .	23
5.3	Multiaxial Dynamics Changes Due to TEVAR . . . . .	25
5.4	Helical Morphology for Type B Dissections . . . . .	26
5.5	TEVAR Influence on Helical and Cross-Sectional Morphology for Type B Dissections . . . . .	27
<b>6</b>	<b>Summary of Results</b>	<b>29</b>
<b>7</b>	<b>Discussion</b>	<b>30</b>
<b>8</b>	<b>Future Work</b>	<b>32</b>
	<b>References</b>	<b>34</b>
<b>II</b>	<b>Appended Papers A-E</b>	<b>41</b>

# Part I

## Extended Summary

### 1 Background

#### 1.1 Introduction

As reported by the World Health Organization, cardiovascular diseases are the leading cause of death globally, accounting for about a third of all deaths each year [1]. A subset of these diseases is vascular diseases. This thesis focuses on two of them, namely, *thoracic aortic aneurysms* and *thoracic aortic dissections*. Disease pathology and pathophysiology will be elaborated on more in Section 1.2.2. One treatment option for these diseases is Thoracic Endovascular Aortic Repair (TEVAR), which involves placing one or multiple implants on the luminal surfaces of the vascular system. These implants are referred to as *stent grafts* or *endografts*. However, there are several aspects that highly influences the outcome of the intervention, and among these that the implant is correctly sized and placed, and that the long term integrity of the structure is secured. Incorrect endograft placement or sizing can lead to complications such as:

- Malapposition of the endograft at the proximal landing zone, also called *bird-beaking* because of the wedge shape created at the inner curve, as seen in Figure 1.1A [2].
- Unintended leakage of blood through or around the endograft: *endoleaks* [3].
- Migration of the endograft. This occurs when the device is moved from its intended placement, due to hemodynamic forces. Oversizing can be an important factor for this type of complication [4].
- Device collapse due to in-folding of the proximal end of a malapposed endograft [5].

The other aspect, the long-term structural integrity of the endograft is dependent on myriad of factors (chemical, biological, and mechanical, *etc.*) and can cause material failure. Cyclic multiaxial loading of the vessels and implants due to cardiac and respiratory motion can cause fatigue damage to the implants which can lead to component failure, see Figures 1.1B and 1.1C. This is when one or several components of the endograft fractures. Important to note is that component failure is only equal to a clinically relevant failure if enough critical components break so that the device to collapses [6]. For example, fracture of one strut of the stent may have no clinical complications (but fracture in several may cause the endograft to malperform), or wear-damage of the graft material may cause endoleaks. Here, it is crucial to rely on realistic boundary conditions derived from the motion of the vascular system in order to make durable device designs.

Ever since x-ray was invented over hundred years ago, non-invasive tools for diagnosis and treatment support have grown increasingly advanced. Today imaging systems are fundamental tools before, during and after interventions. In a strive to provide tools for a high-resolution description of the complex dynamics of the luminal surfaces of blood

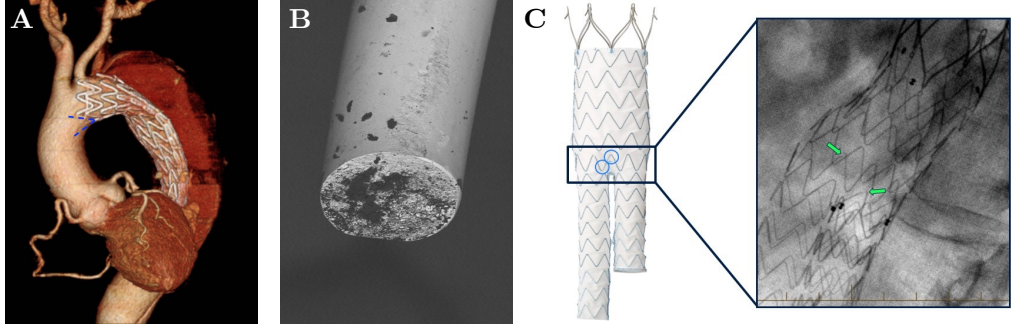


Figure 1.1: Figures show examples of complications that may, or may not, be clinically relevant depending on severity and extent. Figure A shows device malapposition (bird-beaking) at the proximal landing zone (as indicated with blue lines), Figure B shows a single strut failure in a scanning electron microscope, and Figure C shows two strut fractures (indicated with green arrows) for a bifurcated stent graft used to treat abdominal aortic aneurysms. Figures B and C are Figure 17.8 (left) and Figure 17.1 in [7], respectively.

vessels, semi-manual modeling can be performed directly from 3D imaging data. Fully automatic segmentation algorithms based on artificial intelligence and machine learning are emerging. However, it will probably take years before they can reliably and accurately be used to replace the semi-manual methods used in this thesis. The higher level of fidelity is crucial for dynamic studies since the movements, and deformations, can be very small. With this said, it is today motivated to perform the tedious process of manual modeling. Previous work describing vessel motion has been largely focused on centerline and cross-sectional changes of the thoracic aorta [6]. However, since the endografts *in situ* in fact are located directly at the luminal vessel surfaces, there is a need to describe these surfaces explicitly with high accuracy. Additionally, different diseases alter the conditions in terms of lumen configuration, pressure/flow distributions and luminal surface morphology. Patient-specific description of these surfaces is crucial to further advance treatment through improvement of interventions and devices in the future.

### 1.1.1 Purpose, Aims, and Research Questions

The overall purpose, to improve the outcomes of interventions and ultimately the quality of life of treated patients, of this thesis can be divided into three aims: 1) research and establish new knowledge and understanding about thoracic aortic pathology and morphological implications on pathophysiology, 2) support clinicians in their treatment planning (choosing of devices and device placement), and 3) provide medical device manufacturers with more realistic boundary conditions to assist design improvements. These three aims can be reached through geometric modeling and development of integrated and well-validated methodologies to better describe the intraluminal surfaces of thoracic aortas. By doing so, anatomy, physiology, pathology, and pathophysiology can be better described and understood, mechanically as well as clinically. An overview of how the modeling ties to the aims is seen in Figure 1.2. Breaking down the aims for this specific

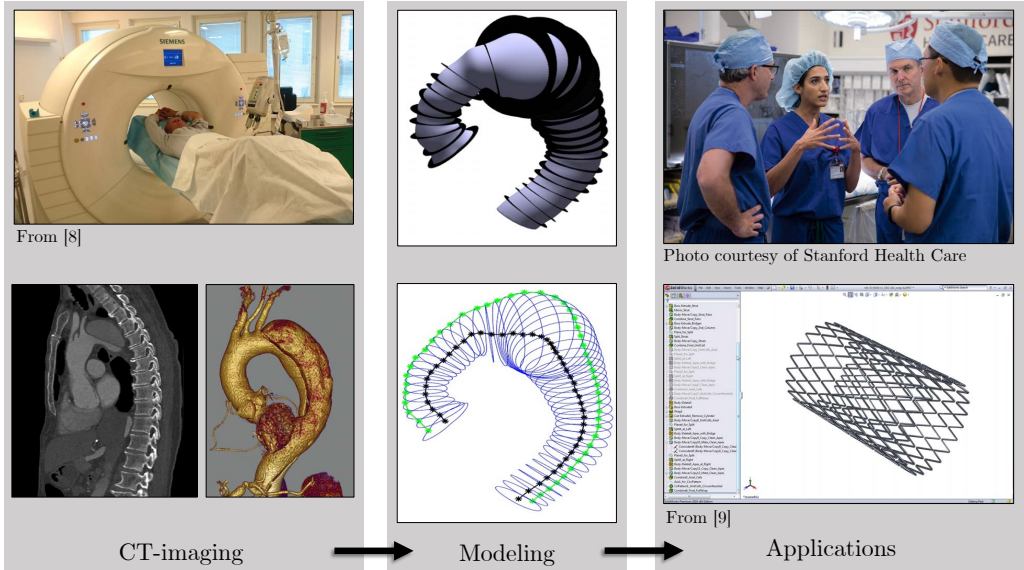


Figure 1.2: Figure shows an overview of the overall workflow from imaging, via modeling and surface description, to use as a pre- or intraoperative tool for clinicians, and boundary condition for device designers, respectively. Top left, top right, and bottom right are attributed to [8], Stanford Health Care and [9], respectively.

project, the following research questions are formulated:

- Develop and validate an automatic cross-sectional slicing algorithm to quantify time-varying thoracic surface quantities for single and dual lumen configurations. Following this, apply the algorithm on patient-specific geometries. This part is presented in **Paper A** with the application on longitudinal surface curvature for static cases and in **Paper D** for description of helical morphology of the true lumen in type B dissections.
- Investigate if endograft malapposition can be predicted preoperatively based on geometrical features. This application is described in **Paper B**.
- Study how endografts and TEVAR influence the multi-axial dynamics of the thoracic aorta. This is presented in **Paper C**.
- Study how endografts and TEVAR influence helical and cross-sectional morphology for dissected thoracic aortas. This is presented in **Paper E**.

Figure 1.3 visualizes how the included research papers in this thesis are connected.

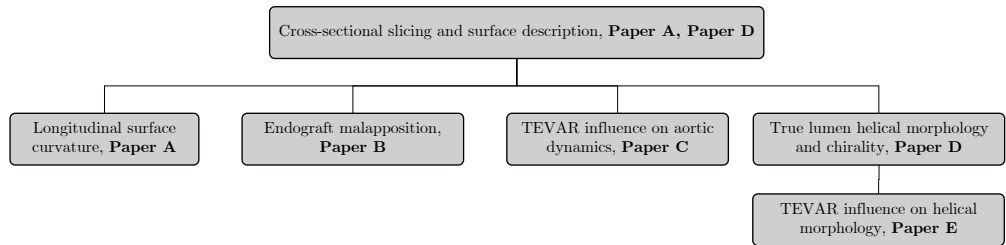


Figure 1.3: A schematic overview of the relationship between conducted research and appended papers in this thesis. By establishing the methodology framework for cross-sectional slicing and surface description, studies on clinical applications can be performed.

### 1.1.2 Limitations

The scope of this thesis is limited according to the following list:

- The vessel segment studied is exclusively the human thoracic aorta.
- Only two types of pathologies of the thoracic aorta are considered: aneurysms and dissections, and no non-diseased thoracic aortas are included.
- Patients included are retrospectively recruited from studies where all patients gave written consent and was approved by Stanford’s Institutional Review Board for human subjects research.
- Among treatment options, only TEVAR is considered when studying morphological and dynamic changes of the thoracic aorta due to interventions.
- Only geometric modeling of the luminal surfaces are to be performed. This does not involve solid modeling of the vessel wall nor simulations of blood flow.

## 1.2 Anatomy, Pathology, Interventions, and Devices

### 1.2.1 Thoracic Aortic Anatomy

The thoracic aorta is the most proximal vessel of the human vasculature, originating from the aortic valve of the heart and ending when passing through the diaphragm, as seen in Figure 1.4. The thoracic aorta has three defined portions: the *ascending aorta*, the *aortic arch*, and the *descending aorta*. The ascending aorta begins the origin of the *right and left coronary arteries* (that supply the heart muscles with blood) just distal to the aortic root and ends at the *brachiocephalic artery* (BA). The BA supplies the right arm and part of the head with oxygenated blood and in the normal configuration the BA marks the proximal limit of the aortic arch. The *left common carotid artery* (LCCA) also branches off from the aortic arch and supplies the head with blood along with the BA. Finally, the *left subclavian artery* (LSA) marks the distal end of the aortic arch. The LSA is the proximal end and the diaphragm the distal end of the descending aorta [10].



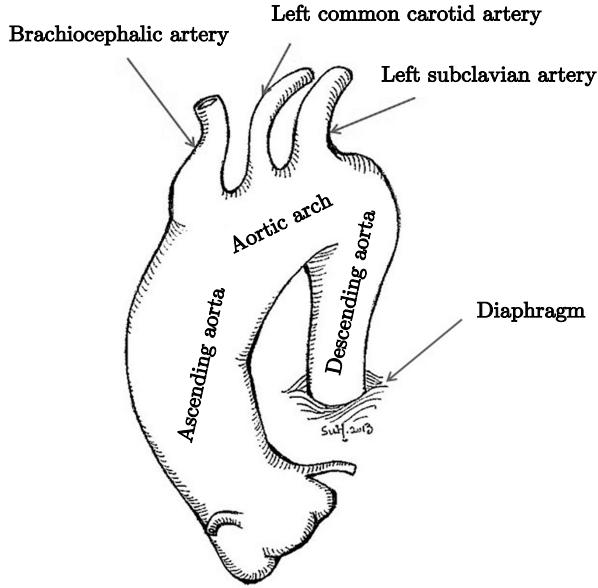


Figure 1.4: Illustration of the thoracic aortic anatomy including branch vessels and segments. The left and right coronary arteries are seen close to the aortic root at the proximal end of the ascending aorta (not annotated).

### 1.2.2 Thoracic Aortic Pathology

As presented in the limitations (Section 1.1.2), the pathologies included in this thesis are thoracic aortic aneurysm and thoracic aortic dissection, see Figure 1.5.

*Thoracic aortic aneurysm* is when the vessel wall is locally weakened and the cross-sectional diameter of the vessel is more than 50% larger than normal. The dilation may grow over time, with an increasingly higher risk for rupture. Today the criterion for intervention is if the aneurysm diameter is larger than 5.5 cm or 6.5 cm for the ascending and descending thoracic aorta, respectively [11–13]. However, individual and more sophisticated criteria based on local rupture risk found by mechanical modeling of the vessel wall have been proposed [14–16]. Such methods could potentially be implemented and treatment options are open surgical repair or endovascular repair.

*Thoracic aortic dissection* occurs when blood leaks through a tear in the intima, the innermost layer of the vessel wall. The leakage is contained within the media, the middle layer, or in the interface between the media and adventitia, the outermost layer. In both cases this creates a parallel lumen called a false lumen, see Figure 1.5B. The false lumen gets pressurized by the direct connection to main blood flow, and the pressure causes the original channel, the true lumen, to partially collapse decreasing the perfusion. The decreased perfusion may lead to ischemia, organ failure, and the damaged vessel wall presents a rupture risk. Treatments of dissections are either medical or through the same procedures as for aneurysms [12].

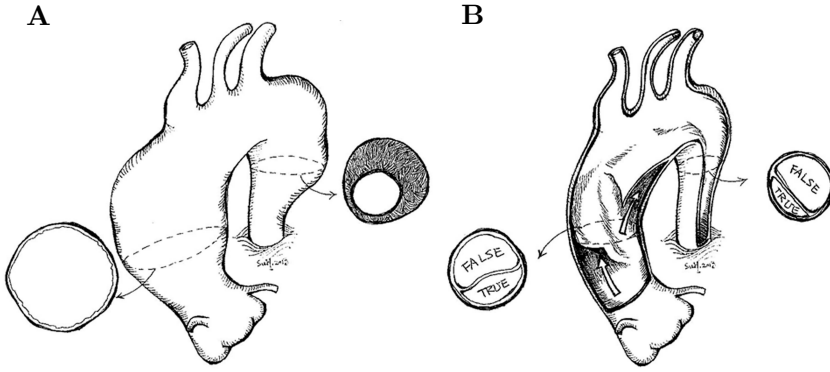


Figure 1.5: Illustrations of thoracic aortic pathologies, with thoracic aortic aneurysm of the whole thoracic aorta (Figure A), and thoracic aortic type A dissection with an intimal tear in the ascending aorta (Figure B).

As seen in Figure 1.6, there are different classifications of thoracic aortic dissections. Those involving the ascending aorta are referred to Stanford type A or DeBakey type I or II, and those involving only the descending portion as Stanford type B or DeBakey type III. Throughout this thesis the Stanford classification is used.

In general, a dissection is considered acute the first 14 days after onset of symptoms, and then chronic [17], a definition that has been suggested to need refinement [18]. The acuity of an aortic dissection highly influences the properties of the vessel wall, and therefore also the remodeling potential when treated with an endograft [19, 20].

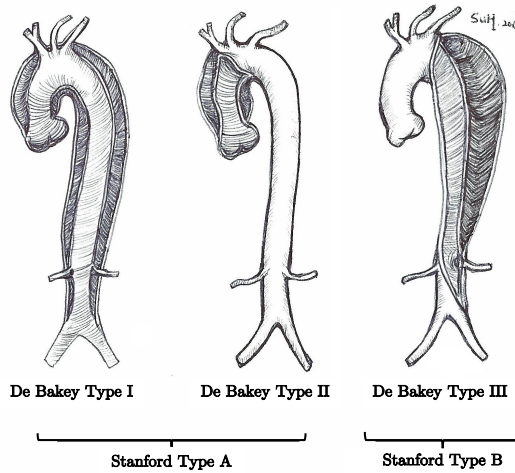


Figure 1.6: Illustrations of different types of thoracic aortic dissections, and their classifications using the DeBakey and Stanford conventions, respectively.

### 1.2.3 Endovascular Interventions and Devices

The previously presented diseases can be treated in different ways: medically, through open surgical repair or endovascular intervention [21]. Within the limitations of this thesis (Section 1.1.2), the procedural details and background are only further explained for TEVAR. Also, a brief description of *endografts*, the type of implant used in these interventions, is presented.

Thoracic endovascular aortic repair is a minimally invasive intervention where access to the vascular system is created through one or several punctures in the groins. For complex procedures, access to the vascular system may also be gained through the arms [21]. Guided by 2D x-ray imaging, the vascular surgeon or interventional radiologist, navigates from the incision through the vascular system with guidewires to access the desired site of device deployment. The endograft is tightly folded into a small catheter and delivered endovascularly, hence the name. When the crimped endograft arrives at the correct location, it is deployed (*i.e.*, unfolded), creating an artificial vessel, see Figure 1.7. Preoperatively, a computed tomography angiography (CTA) is performed to assist the clinician in selecting the right endograft (type and size) and to plan the intervention steps including identifying the most suitable location for deployment. The main advantages with these interventions are the ability to treat patients who would not be candidates for surgical open repair as well as a shorter recovery time and hospital stay [22, 23].

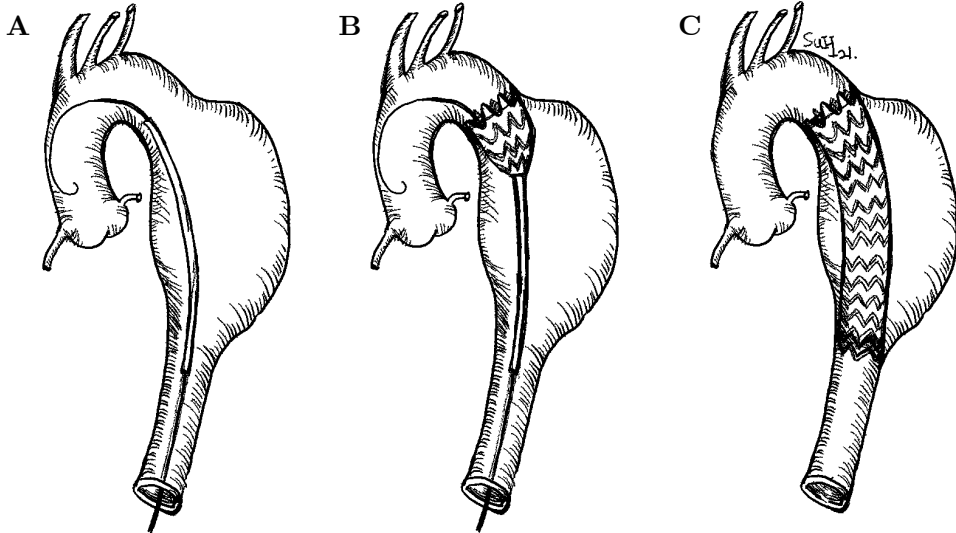


Figure 1.7: Figure depicts the schematic steps of endograft deployment in the case of thoracic endovascular aortic repair of a thoracic aneurysm in the descending aorta. In Figure A the guidewire and catheter have been inserted. The endograft is crimped into the catheter and is in Figure B partially deployed. Finally, in Figure C the endograft is fully deployed and the guidewire is removed.

The implanted devices in these cases are endografts, with examples seen in Figure 1.8. As said, the endograft serves as an artificial vessel and is made from a tube of medical textile supported by a set of metal rings for radial stiffness. The most common types of textiles used are polyester and polytetrafluoroethylene (PTFE), and the metal rings are normally made from Nitinol. Nitinol is a superelastic nickel-titanium alloy that allows crimping of the endograft into the delivery catheter (and large deformations *in vivo*) without plastic damage [24]. Endografts were introduced for treatment of human vessels in the 1980s and 1990s, and both devices and interventions have been significantly and continuously improved ever since [25–27]. It is important that the improvement continues since both device- and intervention-induced complications still occur. Further advancements rely on breakthroughs in several fields: 1) discoveries in metallurgy and medical textiles to allow for improvements of the materials in the endograft components to achieve better durability, 2) improvement of imaging quality and modeling methods to better describe boundary conditions, and 3) more sophisticated tools for preoperative planning to allow for better procedural outcomes.



Figure 1.8: Figure displays a variety of endografts intended to be used in endovascular surgery. Photograph from [28].

## 2 Geometric Modeling of Aortic Surfaces

### 2.1 Imaging and Segmentation

Medical imaging gives the possibility to, non-invasively, visualize and describe internal anatomy and physiology. Over the years, several imaging modalities have been introduced with the most common being: radiation based (x-ray and positron emission tomography), ultrasound, and magnetic resonance imaging. The medical images used in this thesis are all from x-ray sources, namely computed tomography angiography. Computed tomography (CT) creates a 3D volumetric description of the body with high spatial resolution. This is achievable since the x-ray tube and the detector array on the other side of the patient are allowed to rotate, and the examining table to translate. By rotating the source-detector pair a full 360° field of view can be created. By also moving the patient through the static part of the scanner (as seen in the top left corner of Figure 1.2) a cylindrical domain can be described. Angiography (the A in CTA) means that the target for the scanning is the vascular system, and to enhance the attenuation of the blood, contrast fluid (normally iodine for x-ray) is injected intravenously. When analysing the dynamics of the aortic luminal surfaces, it is important to know at what instant of time during the cardiac cycle the image is acquired. To ensure good temporal accuracy, the heart is monitored with an electrocardiograph and the images can then be extracted at the correct instants of time (prospective gating) or a continuous imaging sequence can be stored, and then sorted based on the cardiac cycle after the scan (retrospective gating).

After the images have been acquired, they need to be segmented and modeled before quantification can be performed. Semi and fully automatic methods for 3D segmentation are getting more and more common and in a few years, hopefully, the fully automatic methods can show adequately good accuracy. With this said, there are a lot of software options for handling the raw imaging files and in this project we have utilized SimVascular, which is an open source tool specifically developed for manual and semi-manual modeling and simulation of the vascular system [29]. The workflow is described in steps, as seen in Figure 2.1. First, the centerlines of the vessels and branches are hand-picked in the 3D volume (see Figure 2.1A). Second, following along these centerlines, 2D segmentation can be performed at certain interval to capture the cross-sections (see Figures 2.1B, and 2.1C). This is a natural way to describe a tubular structure and the result of this can then be lofted to a surface (see Figure 2.1D). Worth noting is that this needs to be repeated for every instant of time studied.

### 2.2 Cross-Sectional Slicing

#### 2.2.1 Single Lumen

The labour intensive work of manual surface modeling can potentially be avoided, using an automatic cross-sectional slicing algorithm. In **Paper A**, an algorithm suitable for single lumen is presented and validated. Single lumen conditions are seen in non-diseased aortas and pathologies such as aneurysms (or when, for example, the outer aortic wall is studied

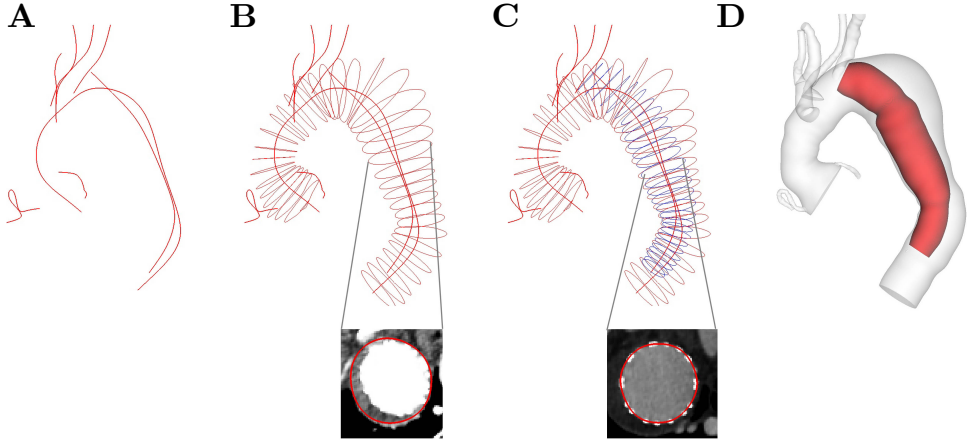


Figure 2.1: Overview of the steps used in the semi-manual modeling tool SimVascular. Figure A shows 3D centerlines for a thoracic aorta, relevant branches and an endograft in the descending portion. Figures B and C show 2D cross-sections of the thoracic aorta and endograft, with examples from modeling of respective cross sections. Figure D shows a rendering of lofted surfaces based on contours (aortic luminal surface in light grey, and endograft surface in red).

instead of the true and false lumina in dissected cases). It is dependent on a 3D triangulated stereolithographic surface (STL file format) as input and outputs a computational grid in the form of centerlines and 2D cross-sections that are structured similarly to the output from SimVascular. In brief, the cross-sectional slicing is mimicking the workflow of the manual segmentation process: creation of initial 3D centerline, cross-section creation, form a new centerline, Fourier smoothing of new centerline, second-generation cross-sections and then iteration of these steps to improve accuracy [30, 31]. The initial centerline is created using a custom made stepping algorithm minimizing the cross-sectional area of proxy-cross sections with varying orientation within the vessel, see Figure 2.2. One proxy cut plane at location  $C_i$  is defined with the the normal  $\hat{n}_i(\theta, \varphi)$ , where the angles are varied:  $\theta \in (-\frac{\pi}{2}, \frac{\pi}{2})$  and  $\varphi \in (0, \pi)$ . The optimal plane orientation and contour at location  $i$  are found by minimizing the area of the contour as described in Equation (2.1).

$$A_{\min,i} = \min_{\theta, \varphi} \int_0^{2\pi} \int_{C_i}^{\sigma_i(\theta, \varphi)} dr d\beta, \quad (2.1)$$

where  $\beta$  is the circumferential direction,  $r$  is the radial direction, and  $\theta$  and  $\varphi$  are the altitude and azimuth angles for the plane normal, respectively. The minimal area is found for a pair of optimized angles  $\hat{\theta}$  and  $\hat{\varphi}$ , which gives the corresponding contour  $\sigma_i(\hat{\theta}, \hat{\varphi})$ . The corresponding numerical algorithm splits the cross-section into triangles circumferentially and then uses the Shoelace formula (Gauss's area formula) to compute the area for each triangle [32]. By summation of all triangle areas the cross-sectional area is finally found. Starting at the proximal end of the surface model, this procedure is

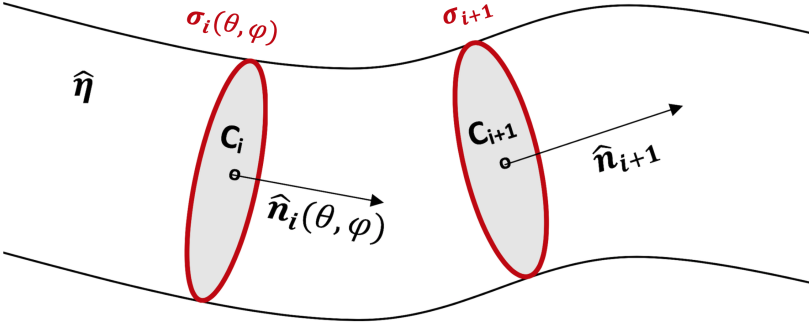


Figure 2.2: Visualization of two consecutive cross-sections found to define the initial 3D centerline.  $C$  represent centroids and  $\sigma$  contours.  $\hat{n}$  and  $\hat{\eta}$  represent the contour, and surface normals, respectively. Using a stepping algorithm, the optimal cross-sections are found along the whole length of the thoracic aorta.

repeated along the whole length by stepping distally. By connecting the centroids of the found contours, the initial 3D centerline is defined.

The details of the following iterative process are described in **Paper A**. Multiple iterations of centerline forming, centerline smoothing and cross-sectional slicing are performed automatically. In some locations, the tortuosity and diameter of the aorta may cause adjacent cross-sections to overlap intraluminally. At the end of each iteration, each set of contours is checked for overlap, and if present, the overlaps are pairwise fixed (by adjusting the pair of normals of the contours to relocate the intersection extraluminally), starting with the worst case of overlap within the set.

### 2.2.2 Dual Lumen

The methods and algorithm described in Section 2.2.1 apply to where the aortic surface can be described by a single tubular surface model. However, as described in Section 1.2.2 in the case of dissections, the cross-sectional slicing algorithm needs to handle two lumina to comprehensively describe the true and false lumen surfaces. In **Paper D** the single lumen methodology is therefore generalized to input dual lumen in the form of two separate 3D surfaces. First, the same steps for cross-sectional slicing are performed on the whole lumen (that is the outer aortic wall representing the union of the true and false lumina). In the last iteration, the surface model of the true lumen is co-located inside the whole lumen and simultaneously sliced. On each cut plane, two contours will therefore be sliced and outputted, as seen in Figure 2.3. The cross-sectional slicing of dual lumen allows for detailed studies including interluminal coupling such as helical morphology.

## 2.3 Lagrangian Formulation of Surfaces

Now, the surface geometries are defined, but to allow for time-dynamic and pre- *versus* post-TEVAR comparisons the surface needs to be described in a Lagrangian cylindrical

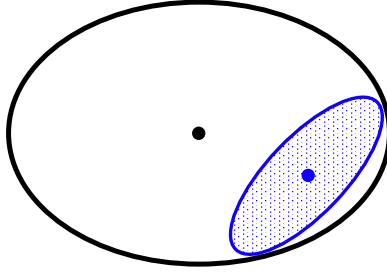


Figure 2.3: Figure depicts a pair of example cross-sections after dual lumen cross-sectional slicing with whole aortic contour and centroid in black, and true lumen contour and centroid in blue.

coordinate system so that material points can be tracked. This natural description of tubular anatomic structures has previously been used in work by Fata, Smith and Lundh [33–35]. In this thesis, methods are based on Lundh’s methods [35], and in the case of dual lumen input, the Lagrangian coordinate system is applied to the whole lumen. This means that longitudinal positions on the true lumen surfaces are described as positions along the centerline of the whole lumen. This is important so that the whole and true lumen surfaces have a common coordinate system to allow for comparison of the lumina at distinct positions. The origin of the coordinate system is defined at a bifurcation between a branch vessel, in this case the LCCA, and the whole lumen surface, see Figure 2.4.

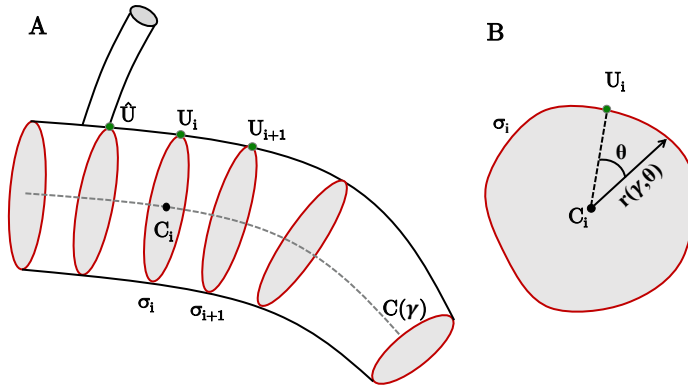


Figure 2.4: Figure displays a schematic description of the Lagrangian cylindrical coordinate system. Figure A shows the longitudinal extent of the coordinate system for a vessel that schematically represents a thoracic aorta.  $\hat{U}$  marks the origin at a bifurcation of a branch, and based on this, the anatomical marker guideline formed by  $\hat{U} \dots U_i \dots U_n$ .  $C$  denotes the centroids and  $\sigma$  denotes the contours. Figure B shows cross-sectional view for contour  $i$ .  $\mathbf{r}$  is the radius and  $\gamma$  and  $\theta$  are the longitudinal and circumferential positions, respectively.



Other markers at, for example, the location of branches or endograft ends are useful for defining regions in the analysis, as described in Section 2.4, and all made possible through the use of the Lagrangian coordinate system description. Each material point on the surface is assigned a longitudinal and a circumferential index and could be viewed as a transformation from a surface in 3D Cartesian coordinates to a 2D cylindrical coordinate system, where the radii are expressed as a function of  $\gamma$  and  $\theta$  as seen in Figure 2.4. The grid is built using linear interpolation based on the input contours from the cross-sectional slicing algorithm and centerline and longitudinal and circumferential resolution can be set depending on needs. For example, to be able to compare a geometry pointwise between two time instances the two models need to have the same resolution. Here it is assumed that the grid interval is slightly stretched from one configuration to another if the surface is stretched, and that this stretch is equally distributed along the whole length and circumference, respectively. The stretching can due to vessel wall anisotropy, neighbouring anatomy, and varying luminal pressure be uneven along the length of the studied segment. To accommodate for this uneven stretching of the grid interval, application of dynamic time warping methodologies is in some cases used to ensure that the same material points are compared [36–38]. In short, these methods minimize the sum of the Euclidean distances between the signals to match peaks.

## 2.4 Quantification Domain

### 2.4.1 Longitudinal Region of Interest

Fiducial markers, in addition to the LCCA, used in this thesis are: Right coronary ostium and BA to define the ascending aorta, BA and LSA to define the aortic arch, and LSA and the most distal intercostal artery to define the descending aorta (*cf.* Section 1.2.1). In **Paper A** the whole thoracic aorta (ascending, arch and descending) is studied, whereas in **Paper C** the portions are separately studied. In **Paper C** markers for the endograft ends are used to define the stented region, specifically studied, see Figure 2.5. In **Paper B** the proximal end of the endograft and the landing zone are of extra importance to define the bird-beaking metrics (see in Section 5.2). In **Papers B, C and E**, the endograft end markers in relation to fiducial markers are used to determine the corresponding locations prior to and after intervention. For example, if the proximal end of the endograft is situated 1 cm distal to the LCCA along the centerline arc length postoperatively, the stented region is assumed to start 1 cm distal to the LCCA in the preoperative model as well. An example where the proximal end of the region is based on pre-TEVAR geometry, and the distal end is based on the post-TEVAR geometry is seen in Figure 2.5.

The longitudinal marker can be placed at any given longitudinal position, or be decided by other fiducial markers or features. For example in **Paper D** and **Paper E** the proximal end of the region is defined at the longitudinal position 5 cm distal to the LCCA or at the location of the intimal tear if this is more distal. In **Paper D** the distal end of the region is defined at the end of the provided images (about the level of the intercostal artery at the diaphragm) and in **Paper E** the distal end of the endograft in the post-TEVAR is used to define the distal end of the region, as seen in Figure 2.5.

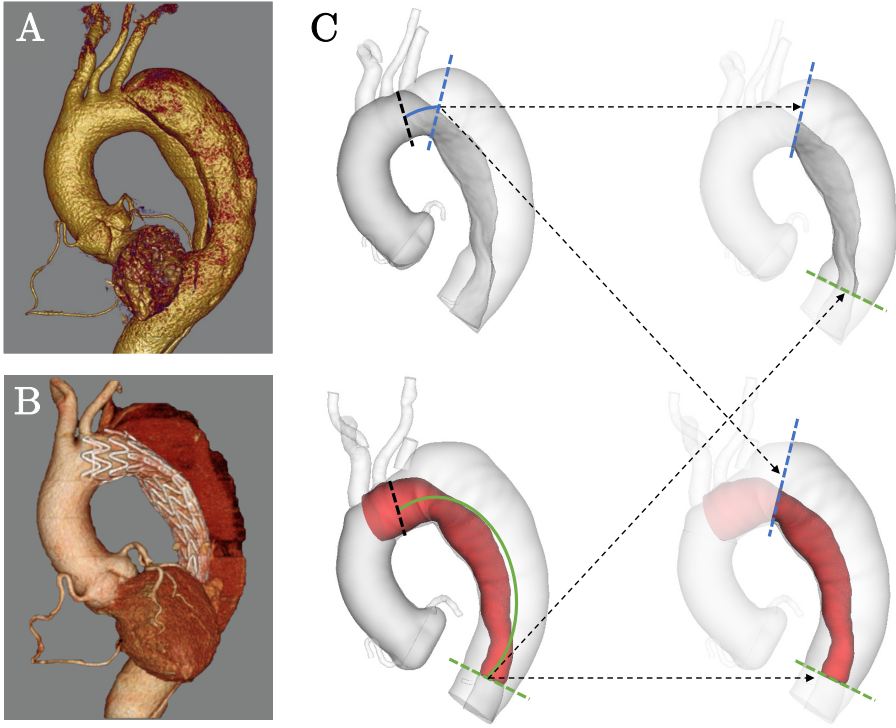


Figure 2.5: Figure A and B display renderings of CT data for pre- and post-TEVAR, and Figure C shows how the Lagrangian coordinate system is used to form a comparable region for pre- and post-TEVAR in a dissected thoracic aorta. In this case a longitudinal fiducial marker 5 cm distal to the LCCA is placed in the pre-TEVAR model (as seen in blue) and the centerline distance to the distal end of the endograft is found in the post-TEVAR model (green). By transferring the pre-TEVAR marker to post-TEVAR and *vice versa*, a common region of interest is defined as visualized in the rightmost column.

### 2.4.2 Longitudinal Surface Paths

To represent certain circumferential sections of the aortic surfaces in a more compact way, metrics are extracted along *longitudinal surface paths*. To start off with, the anatomic marker guideline (see  $Y_1 \dots Y_i \dots Y_n$  in Figure 2.4) represents the reference circumferential coordinate, and is indeed a longitudinal surface path spanning the whole longitudinal extent of the model. In this way, in **Paper A** and **Paper C** the inner and outer surfaces of the thoracic aorta are represented by inner and outer surface paths, which are found in the following way: relying on the Lagrangian grid, the inner path is found as the shortest path between the levels of the right coronary artery and the intercostal artery fiducial markers, parallel to the anatomic marker guideline in the 2D coordinate system. The outer path is then chosen as the path  $180^\circ$  shifted from the inner path. The inner and outer surface paths and the centerlines are displayed in Figure 2.6. In **Paper B**

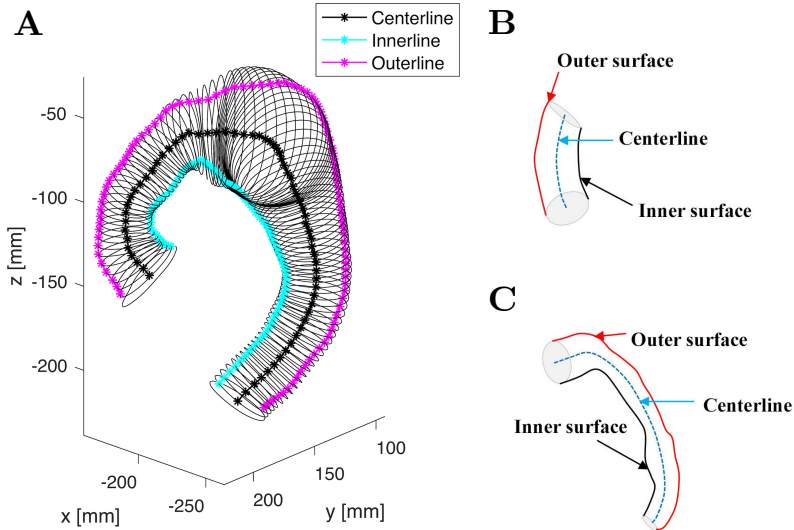


Figure 2.6: Figure shows the definition of inner and outer surface paths. Figure A shows the the inner and outer surface paths used in **Paper A** denoted as "Innerline" and "Outeline", respectively. In Figures B and C, the inner and outer surfaces are represented by paths on the ascending and stented portions as defined in **Paper C**.

the methodology for finding the inner path is in this case slightly modified compared to the surface curvature case in **Paper A** and **Paper C**. Instead of finding the shortest parallel path to the anatomic marker guideline, the center of mass (COM) for the thoracic aortic model is found located axially above the right coronary artery. By minimizing the distance of all points on the most proximal contour to the COM, the starting point of the inner path is defined. This point is then projected onto the distal contours to form the full inner path in the same manner as when defining the anatomic marker guideline based on the LCCA ostium, previously described. The inner path of the endograft is then found as the shortest distance to the aortic inner path, for each endograft contour at a time. After defined, the paths are smoothed using Fourier smoothing [31] and subsequently used for computation of bird-beak metrics (see Section 5.2).

## 2.5 Metrics Definition

Relying on the Lagrangian formulation for pointwise tracking, and after defining the region of interest (ROI), a series of metrics are computed for different applications: Longitudinal curvature metrics (explicit quantification and estimation of surface curvature), cross-sectional metrics (area, circumference, effective diameter, eccentricity) and helical metrics (helical angle, helical twist and helical radius). These, or combinations of these, are then used to study the different clinical hypotheses presented in Chapter 5.

A natural first application using the Lagrangian grid is to quantify surface curvature explicitly for each point on the surface, in this case in the circumferential and longitudinal directions, respectively. These can be used to compute mean and Gaussian curvature, which have been shown to be related to abdominal aortic aneurysm rupture risk [14, 39]. However, in this thesis, the focus is on longitudinal surface curvature, how it can be accurately quantified and in particular why it is important.

The general formula for curvature reads

$$\kappa = \frac{\|\mathbf{r}'(t) \times \mathbf{r}''(t)\|}{\|\mathbf{r}'(t)\|^3}, \quad (2.2)$$

where  $\mathbf{r} = \mathbf{r}(t)$  is the parametric equation for the curve and primes refer to derivatives with respect to the parameter  $t$ . The curvature formula in Equation (2.2) is here discretized with a circle fitting method ( $\kappa = \frac{1}{R}$ , where  $R$  is the radius of curvature), which allows for implementation of a sliding window to reduce noise. The optimal window size has previously been suggested by Choi and Lundh [31, 35]. Inspired by the circle fitting method, a straightforward method for estimating longitudinal surface curvature from centerline curvature and radii is also investigated. First, the inner and outer surfaces are defined as surface paths as described in Section 2.4.2 and radii are quantified from the centerline to each of the paths. Then the inner and outer local radii are added to the inverse of centerline curvature at each point yielding new radii of curvature. From these, the estimated inner and outer curvatures are computed, see Equations (2.3) and (2.4).

$$\kappa_{\text{outer, est}} = \frac{1}{\left(\frac{1}{\kappa_{\text{center}}} + r\right)} \quad \text{and} \quad (2.3)$$

$$\kappa_{\text{inner, est}} = \frac{1}{\left(\frac{1}{\kappa_{\text{center}}} - r\right)}, \quad (2.4)$$

where  $\kappa_{\text{center}}$  is the local centerline curvature and  $r$  is the local radius while  $\kappa_{\text{outer, est}}$  and  $\kappa_{\text{inner, est}}$  are the estimated curvatures for the outer and inner surfaces, respectively.

The *effective diameter*,  $D_{\text{effective}}$ , is calculated as

$$D_{\text{effective}} = 2 \cdot \sqrt{\frac{A}{\pi}}, \quad (2.5)$$

where  $A$  is the cross-sectional area of the vessel. The cross-sectional area of a contour is indicated as the shaded area in Figure 2.7A. For a fully circular cross-section the effective diameter is the same as the diameter. However, in the case of non-circular cross-sections, the effective diameter is different from the diameter since every point on the parameter has different radii, but it serves as a measure proportional to mean diameter.

From Figure 2.7A the definition of true lumen circumference can also be seen as the length of the blue contour. A group of researchers has proposed that the circumference is the better for computing oversizing compared to diametric measurements [40, 41]. This is something that will be evaluated for thoracic pathologies with regards to complication risks as a part of the proposed future work (Section 8).

The *eccentricity* is computed as:

$$\varepsilon = \sqrt{1 - \left(\frac{b}{a}\right)^2}, \quad (2.6)$$

where  $b$  and  $a$  are the minor and major axes of a cross section, respectively. An eccentricity level of 0 corresponds to a perfect circle (since  $b = a$ ) and, on the other hand, the eccentricity approaches 1 as the cross section gets increasingly oblong.

Metrics to describe helical morphology are defined using two methods, the surface-based method (SBM) and the centerline-based method (CBM). In the SBM, the true lumen is defined relation to the surface path of the fiducial marker guideline, as seen in Figure 2.7 where the angular position ( $\alpha$ ) and the helical radius (red arrow) are defined. The helical angle is then defined as the difference between angular position at the distal and proximal ends of the ROI. Helical twist is then defined as the change of angular position in a sliding window within the ROI. An evaluation of optimal sliding window size is described in Chapter 3. The CBM is similar but does not rely on the fiducial marker guideline (surface path), but instead on a line that mimics this guideline starting from the LCCA ostium and then in parallel with the centerline. Apart from the different way of defining this line, the quantification steps are the same, however, no cross-sectional information such as eccentricity, area and circumference can be extracted.

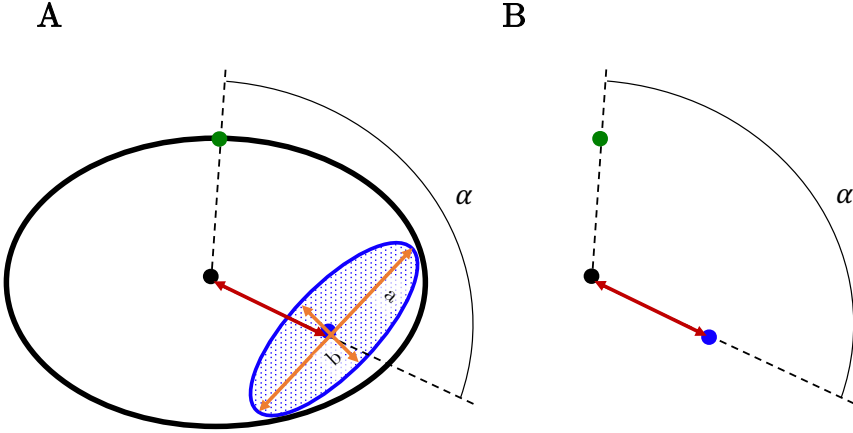


Figure 2.7: Figure displays the methods to extract metrics for the surface and centerline-based methods as defined in **Papers D** and **E**. Figure A shows the surface-based method used to extract angular position,  $\alpha$ , and helical radius, and true lumen cross-sectional metrics (area, circumference and eccentricity), whereas Figure B shows the centerline-based method. Note that the latter only can extract angular position,  $\alpha$ , and helical radius.

### 3 Validation of Models and Methodology

Before applying the developed methods to patient-specific geometries, they need to be thoroughly validated. Within the body of this thesis, two methods validation studies have been performed using phantoms. The purpose of these studies are twofold: 1) to quantify errors introduced and 2) to calibrate parameters. With this said, both validations performed are specific to the metric quantified in each study, longitudinal surface curvature and helical twist, respectively.

#### 3.1 Phantom Design

The method validation utilizes application of the methodology on computer generated phantoms. A phantom is, in contrast to patient-specific geometries, an artificial geometry created for the sole purpose of the method validation. It mimics patient-specific features, but designed based on a mathematically constrained blueprint with known analytic solution. All phantoms for method validations are designed and built in the CAD package CATIA V5 [42]. In **Paper A** three phantoms are used, representing a single aortic lumen in a bent non-aneurysmal case (Figure 3.1A), a straight aneurysmal case (Figure 3.1B), and finally superpositioning of these (Figure 3.1C), respectively.

In **Paper D** the dual lumen cross-sectional slicing algorithm is validated on six whole aortic-true lumen combinations (true lumen as seen in Figure 3.2B inside of the whole lumen as seen in Figure 3.2A) with various levels of analytically defined helical twist. The LCCA is again used as the fiducial marker to form the origin of the Lagrangian cylindrical coordinate system.

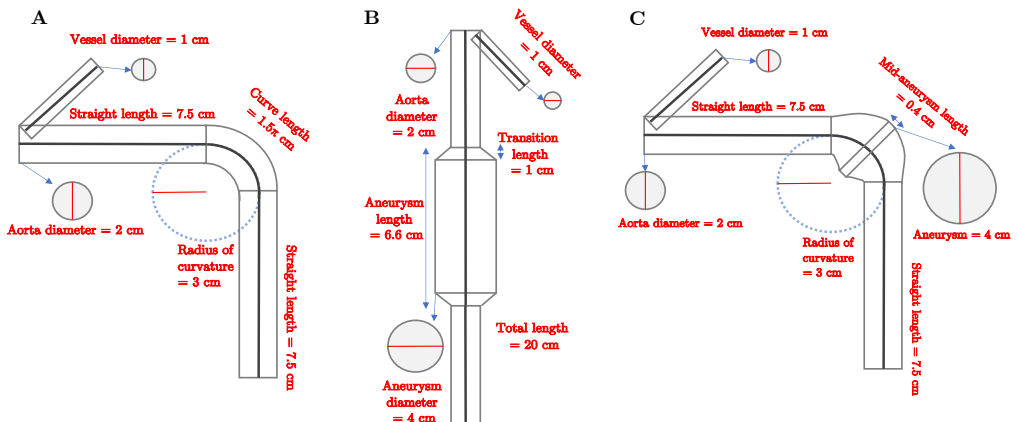


Figure 3.1: Figure displays the three phantoms used for validation of single lumen and longitudinal curvature quantification used in **Paper A**. Figure A shows a non-aneurysmal case with a  $90^\circ$  bend, Figure B shows an aneurysmal case on a straight centerline, and Figure C shows a phantom where phantoms in Figure A and B are superpositioned.

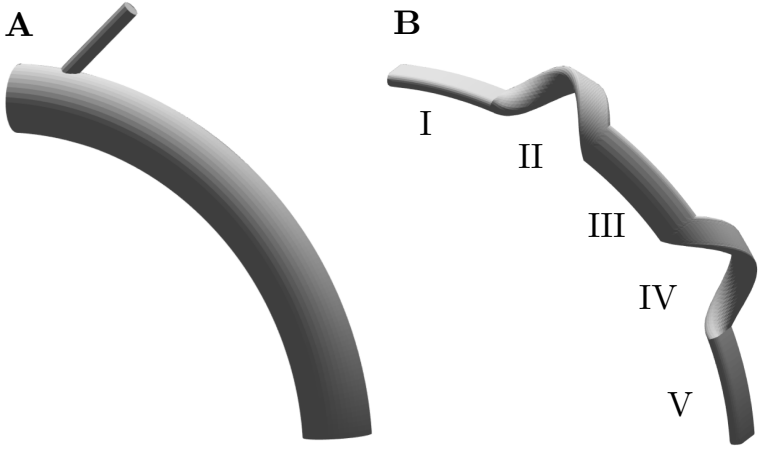


Figure 3.2: Figure displays one out of six whole aortic-true lumen combinations used for validation of dual lumen and helical twist quantification used in **Paper D** with the whole aortic lumen part (A) and the true lumen part (B).

### 3.2 Error Estimation and Parameter Calibration

Depending on the application, different measurements of error is important. For example, in **Paper A** the peak, mean, and RMS (root mean square) errors are computed. The performance is closely linked to parameter settings, and especially with regards to the sliding window size when it comes to surface curvature quantification. The window size chosen is based on research reported in [31, 35]. In the general case a smaller window allows the solution to better follow sharp transitions with the trade-off that it may overshoot in the near-transition regions. In other words, a small window allows for low RMS errors but likely introduces larger peak errors. A small window is also more sensitive to noise, and mean errors are also expected to increase. Large window sizes may be less sensitive to noise, but may also perform worse in near-transition regions. The validation study showed that the curvature was underestimated by 0% to 9% at optimal settings and tuned to be a good trade-off between with regards to accuracy and noise sensitivity. Errors that remain are most likely due to numerical implementation and discretization.

In **Paper D** a similar assessment of accuracy is performed. Here, the peak error is exclusively investigated and used in parameter tuning. In the case of helical twist, no previous study had assessed optimal window sizes (as for curvature) and is therefore carried out, for the surface- and the centerline-based methods, respectively. One phantom comprises of a combination of the whole lumen, and true lumen surface models, as seen in Figure 3.2. Even though the true lumen phantoms included three achiral parts split by a clockwise chiral and a counterclockwise chiral part (as seen in Figure 3.2B), only parts (II-IV) forms the basis for parameter tuning. This to equally weigh together the performance in clockwise, counterclockwise, and achiral parts, as seen in Figure 3.3A.

Because another study has suggested segmentation interval influences the accuracy, the cross-sectional slicing interval is also evaluated, in addition to the window size study [43]. The results for both these parameters are visualized in Figure 3.3B with helical twist quantification being most accurate (when excluding the sharp transition zones) with the settings of cross-sectional slicing interval of 0.5 cm and a window size of 4 cm.

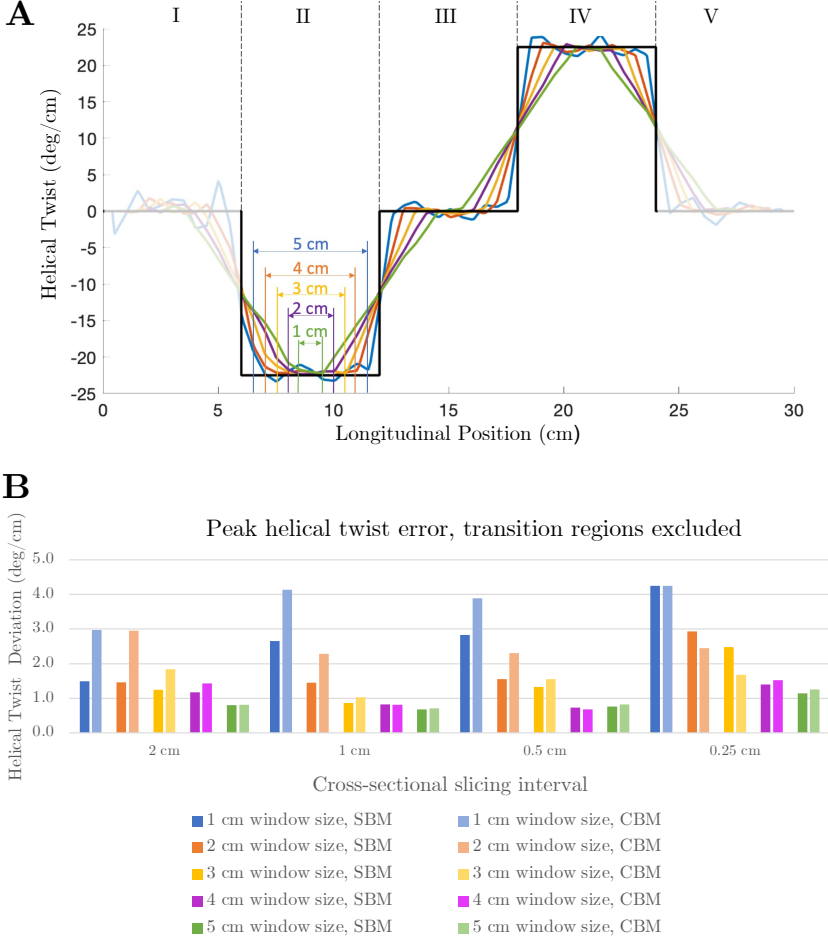


Figure 3.3: Figure displays the results of parameter tuning for helical twist, with regards to peak helical twist error in a region spanning parts II-IV (see Figure 3.2). Figure A shows an example for the 0.5 cm cross-sectional slicing interval, and Figure B shows the result for both the surface-based method (SBM) and the centerline-based (CBM) method.



## 4 Explicit and Estimated Surface Curvature

As previously defined, the explicit surface curvature method correlated well with analytic solutions for longitudinal curvature for the defined inner and outer lines as well as for centerline curvature. The estimation method was working well for phantoms mimicking healthy vessels, but working very poorly for those who represents diseased morphologies, as seen in Figure 4.1. Based on these results, the surface curvature estimation method was not applied to the patient-specific cohort, but instead only the explicit method.

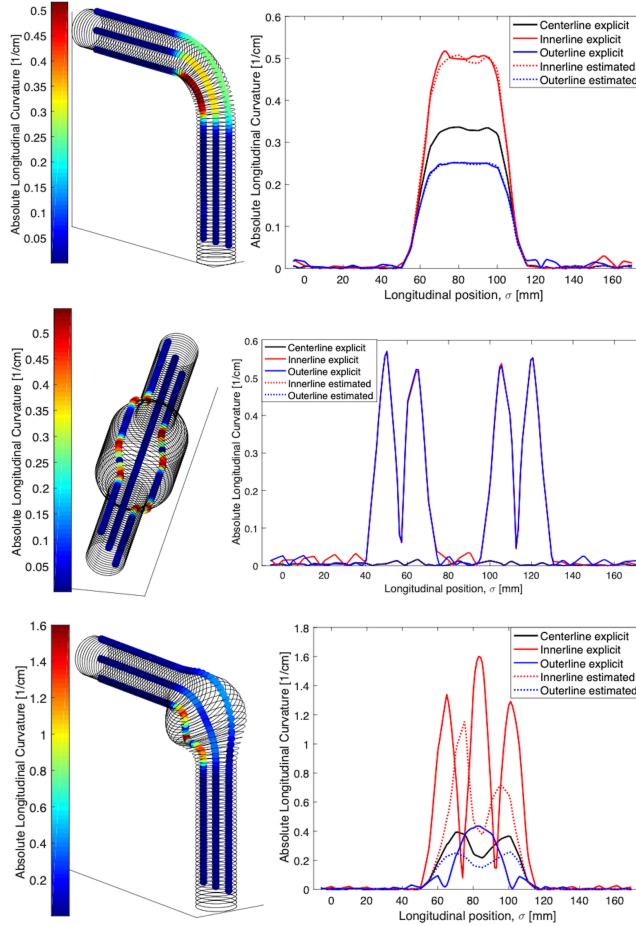


Figure 4.1: Figure shows explicit (pointwise quantified) longitudinal surface curvature along inner and outer lines for the three computer generated phantoms (left column), and comparison between explicit and estimated surface curvature along the length of the same phantom (right column). Note that the surface curvature estimations are indistinguishable from the centerline curvature for the second phantom because the centerline is straight.

## 5 Applications on Patient-Specific Aortas

The established methodology (Chapter 2) was, after validation on phantoms (Chapter 3) applied on patient-specific data with clinically relevant hypotheses. In this chapter, these applications (included in the appended papers) will be summarized. The focus is on geometric features to describe the luminal surfaces and how TEVAR affects the static and dynamic conditions of the thoracic aorta.

### 5.1 Explicit Quantification of Longitudinal Curvature

For a cohort of 37 patient-specific diseased thoracic surfaces, this study confirmed the hypothesis that the inner surface curvature is significantly higher than the centerline curvature (both mean and peak values), and hence important to quantify in order to describe surface conditions accurately. The outer longitudinal surface curvature was not significantly different compared to the centerline curvature for the diseased thoracic aortas, a result that was expected for healthy vessels. This is explained by the influence of aneurysms and dissections, which cause local high areas of surface curvature even on the outer curve. An example of this is seen in Figure 5.1, where the peak inner surface curvature is three times larger than the centerline curvature. Here it is also seen that the inner curvature is more noisy, which is confirmed by the RMS values being significantly greater compared to centerline RMS and outer surface curvature.

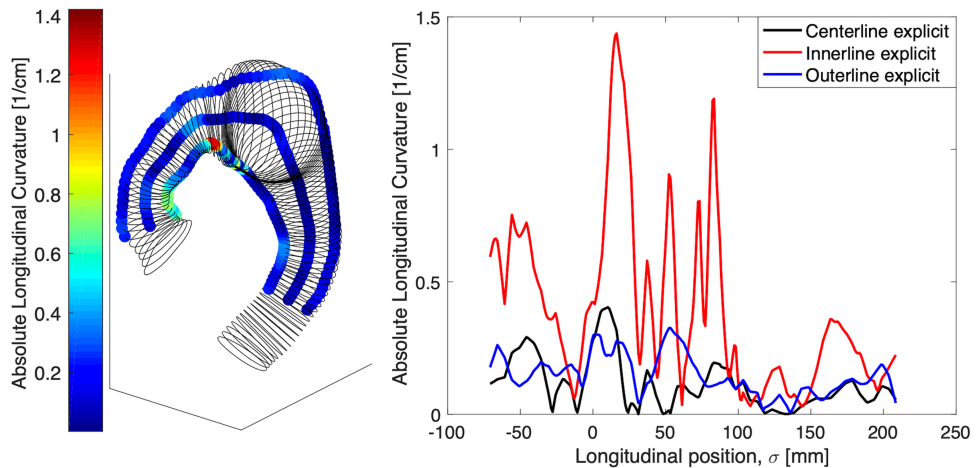


Figure 5.1: Figure shows the absolute longitudinal curvature for one example patient from the 37 patient cohort. Left figure displays it along the surface paths and centerline in the 3D model, and to the right the values are plotted *versus* the longitudinal position based on the centerline arc length.

## 5.2 Endograft Malapposition Prediction

Based on the methods for imaging and modeling described in Section 2.1, thoracic aortic and endograft centerlines and cross-section models were constructed to form the input for this application. Based on the two inner curves defined in Section 2.4.2, the longitudinal region of the proximal landing zone was defined from the point-pair  $g_0$  (proximal end of the endograft) and  $a_0$  (proximal landing point) to the distal point-pair  $g_1$  and  $a_1$  (where the threshold distance between the two curves drops below 3 mm) as seen in Figure 5.2. Bird-beak height (BBH) was defined as the distance between  $g_0$  and  $a_0$ , bird-beak length

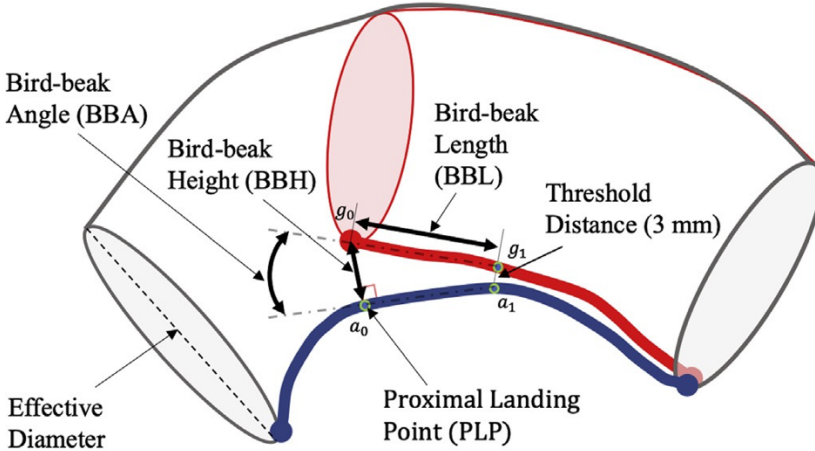


Figure 5.2: Figure displays a segment of the thoracic aorta around the proximal landing zone of the endograft. Bird-beak metrics including bird-beak angle, bird-beak height, and bird-beak length as well as the four points that underlie these metrics  $a_0$ ,  $a_1$ ,  $g_0$ , and  $g_1$  are visualized.

(BBL) as the Euclidean distance between  $g_0$  and  $g_1$ , and finally the bird-beak angle (BBA) according to Equation (5.1)

$$BBA = \cos^{-1} \left( \frac{\mathbf{a} \cdot \mathbf{g}}{\|\mathbf{a}\| \|\mathbf{g}\|} \right), \quad (5.1)$$

where  $\mathbf{a}$  is the vector between  $a_1$  and  $a_0$ , and  $\mathbf{g}$  is the vector between  $g_1$  and  $g_0$ . Preoperatively, the inner surface curvature (quantified using the circle fitting method as described in Section 2.5) as well as the aortic effective diameter were measured at the proximal landing point,  $a_0$ . The level of local oversizing was determined from this by comparing to the specifications of the endograft. In general, an oversizing in the interval of 10% to 20% is recommended for these interventions and too much oversizing (>30%) can be negative with regards to device migration [4, 44].

Using the inner surface curvature and the effective diameter, a unitless product was found (results seen in Figure 5.3). The rationale for defining such a dimensionless metric was based on how tubes are constrained in bending. The inner curve needs to shorten,

and the outer lengthen to fulfil being perpendicular to the centerline. When the outer curve of the endograft was stretched fully, the inner curve could not contract/wrinkle to accommodate for high inner surface curvature and bird-beaking occurs. This application reveals that this preoperative metric was significantly higher in the group with bird-beaking post-TEVAR (grouping with threshold BBH=5 mm). Also, this metric along with the inner surface curvature alone are found to correlate with both BBH and BBA, where the latter agrees with previous findings from Kudo *et al.* [45].

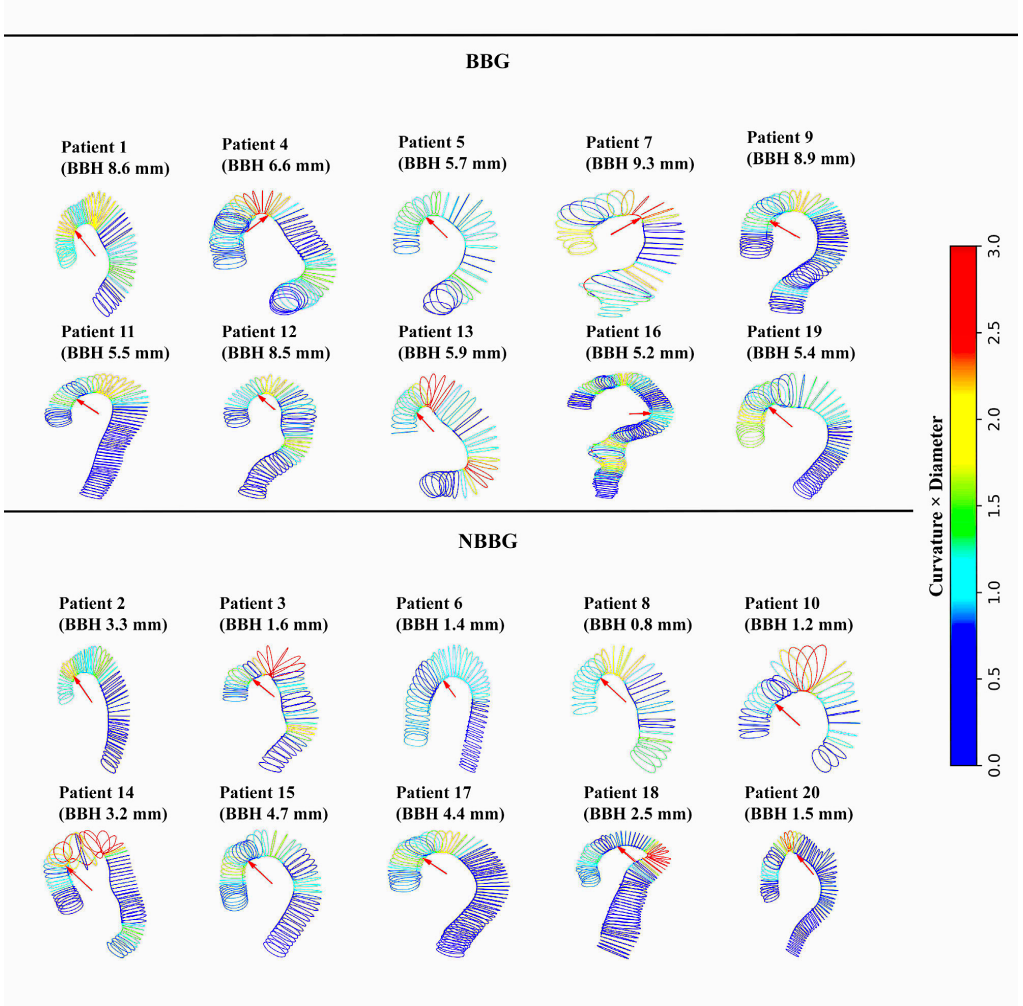


Figure 5.3: Figure shows the preoperative unitless metric (longitudinal inner curvature times effective diameter) for each patient grouped in the bird-beak group (BBG) shown in the top part, and no bird-beak group (NBBG) show in the bottom part.

### 5.3 Multiaxial Dynamics Changes Due to TEVAR

The third application of the presented framework was a study on multiaxial dynamics of the thoracic aorta. Models of thoracic aortas were constructed at ten different instants of time during the cardiac cycle using retrospective gating as described in Section 2.1. This was performed both before and after TEVAR, yielding a total of 20 models per patient. The models were then defined in an Lagrangian cylindrical coordinate system (Section 2.3) to be able to quantify longitudinal surface curvature and effective diameter as described in Section 2.5. These metrics were then extracted and studied in different regions, as described in Section 2.4 and further visualized in Figure 2.6. This analysis revealed how TEVAR affected the cardiac-induced deformation of the different regions of the thoracic aorta, and the results confirmed the hypothesis that the stented portion exhibits a decrease in cardiac-induced deformation from pre- to post-TEVAR.

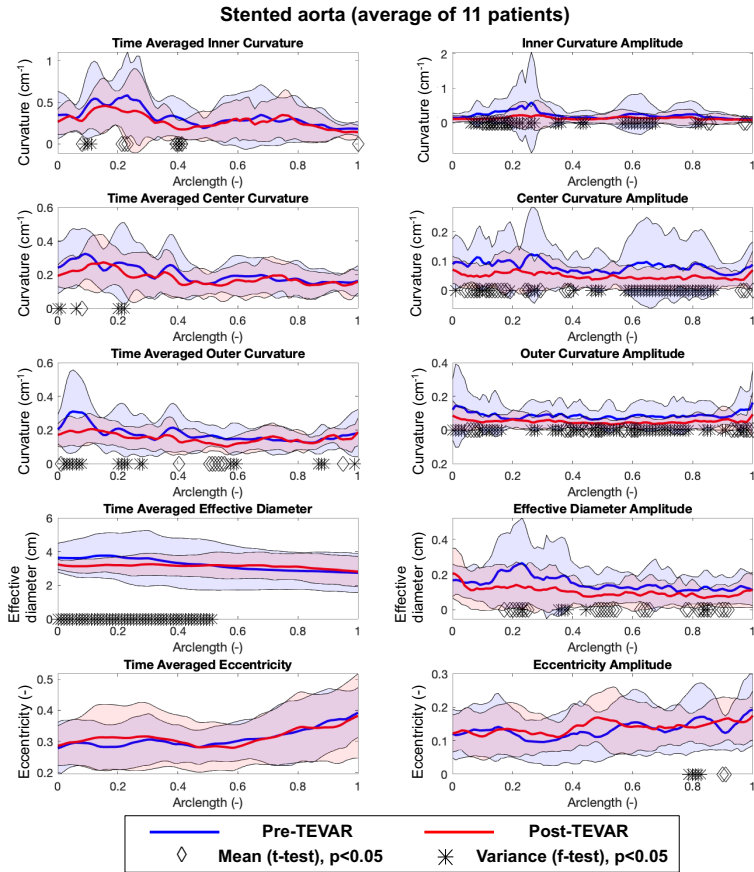


Figure 5.4: Figure shows the results for the stented portion of the aorta, averaged for all 11 patients. The results show the multiaxial dynamics change, with longitudinal curvature and cross-sectional diameter and eccentricity.

## 5.4 Helical Morphology for Type B Dissections

After development of the dual lumen cross-sectional slicing algorithm, the two methods for quantification of helical metrics as described in Chapter 2, and validated in Chapter 3, were applied to a cohort of 19 patients with type B aortic dissection. The results show that the patients clustered into two distinct groups based on the helical angle (the difference between angular position at the distal and proximal end): one where the true lumen was achiral and followed the inner surface of the aorta (helical angle around  $0^\circ$ ), and another where it was right-handed chiral and propagated in a helical manner (helical angle around  $-180^\circ$ ), as seen in Figures 5.5A and B, respectively.

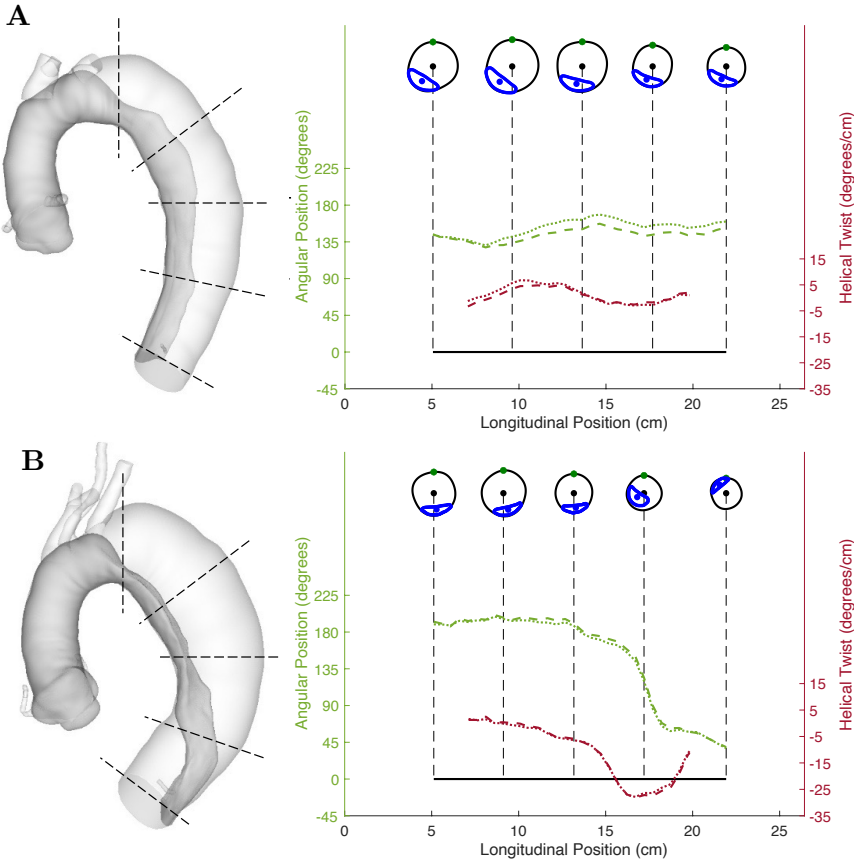


Figure 5.5: Figure displays two representative patients from each of the two clusters with an achiral propagation (Figure A) and a chiral propagation (Figure B). The left column shows the surface models and indicates the approximate locations of the five cross-sectional contours shown in the top of each figure in the right column. In the right column, the angular position and helical twist are shown for both surface-based and centerline-based methods for each patient.

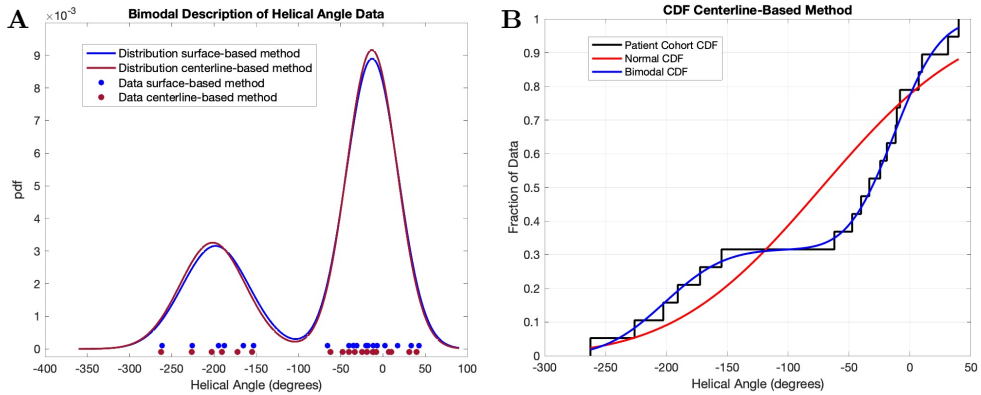


Figure 5.6: Figures displays the probability density function (pdf) for the bimodal description of the data set, and the data (dots along x-axis) (A), and the cumulative distribution function (cdf) for the centerline-based method (B).

A visualization of the data for all 19 patients using both the surface and centerline-based methods are seen in Figure 5.6A. To further investigate the bimodality of the data, the cumulative distribution function of the measured data was compared to a bimodal and a normal description, respectively, as seen in Figure 5.6B. The fact that the bimodal description (blue line) seemed to fit the data (black line) much better than a normal distribution (red line) was supported with the results from a one-sample Kolmogorov-Smirnov test [46]: For the bimodal description, the fit was  $p=0.999$  (SBM) and  $0.996$  (CBM) while the normal distribution model showed  $p=0.127$  (SBM) and  $p=0.208$  (CBM). To make this assessment of bimodality more comprehensive, Ashman's D was computed for all metrics. Ashman's D is a measurement of clean separation between two groups in a bimodal distribution, and all metrics except helical radius were greater than the threshold of 2 for both methods, indicating distinct bimodality [47].

The finding of chiral propagation pattern is similar to other observations in nature such as: biological homochirality (Pasteur [48]), twinning tree trunks (Darwin [49]), and the double helix deoxyribonucleic acid (DNA) structure (Watson and Crick [50]). In the case of spiraling dissections, we speculate it to be influenced by factors presented in previous findings about the aortic root dynamics, the helical blood flow pattern in the aorta but also by the orientation of fibres in the medial layers of the thoracic aorta [51–54].

## 5.5 TEVAR Influence on Helical and Cross-Sectional Morphology for Type B Dissections

By combining the dual lumen cross-sectional slicing algorithm with pre- to post-TEVAR region definition (as described in Chapter 2 and seen in Figure 2.7) the hypothesis of how TEVAR influences the helical and cross-sectional metrics could be tested. Models



were built for 16 patients based on CT-scans before and after TEVAR. By using the SBM introduced in Chapter 2 a comprehensive set of metrics could be quantified. This included helical metrics (helical angle, average and peak helical twists, and average helical radius), and cross-sectional metrics (average true lumen eccentricity, average true lumen area, and average true lumen circumference). Two subgroup analyses were also performed: one based on acuity and one on pre-TEVAR chirality (with a threshold of helical angle  $= -90^\circ$ ). For the cohort as a whole, TEVAR decreased the average helical radius and average true lumen eccentricity, and increased the average true lumen area and average true lumen circumference. The subgrouping based on acuity revealed that the average true lumen circumference does not increase for chronic cases. From the subgroup analysis based on chirality, the distinct grouping between achiral and chiral subgroups found before TEVAR vanished after TEVAR. This is visualized for one case in Figure 5.7, where we can observe some of the effects earlier mentioned; decreased helical radius (the centroids are almost on top of each other post-TEVAR), decreased eccentricity (post-TEVAR is more round), and an increase of true lumen area and circumference. These are all changes that are favourable for flow based on centerline path and cross-sectional shape and area [55–57].

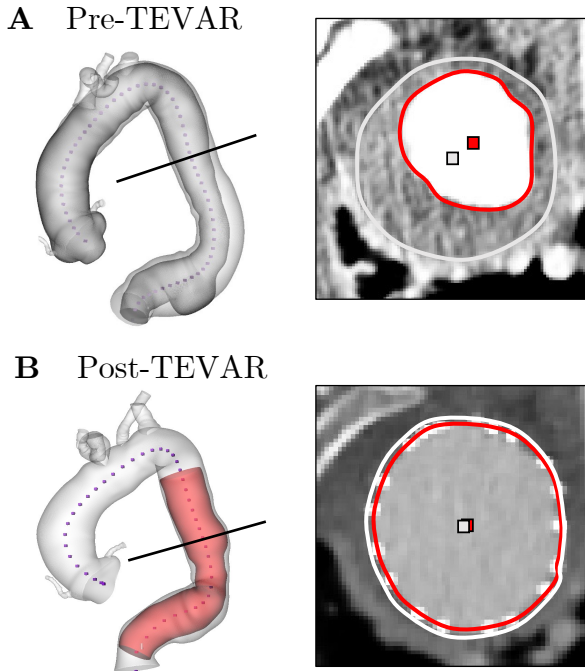


Figure 5.7: Figure shows an example of pre-TEVAR (A) and post-TEVAR (B) geometries. The collapsed true lumen pre-TEVAR is expanded and due to favourable remodeling of the false lumen (which is entirely decimated in this case).



## 6 Summary of Results

The results presented throughout Chapters 3-5 are herein summarized.

Firstly, methods for geometric modeling including a cross-sectional slicing algorithm capable of inputting single or dual lumen configurations were developed to match the pathologies of diseased thoracic aortas. Description in a Lagrangian cylindrical coordinate system allowed for pointwise tracking of the surfaces. A set of metrics to comprehensively describe morphology of luminal surfaces were introduced and validated on phantoms to ensure accuracy before applied to patient-specific cases.

Secondly, based on a phantom study, longitudinal surface curvature can be relatively well estimated based on centerline curvature and radii for phantoms mimicking non-diseased thoracic aortas. However, when applied on phantoms mimicking diseased thoracic aortas, the performance were far from acceptable. Therefore, this estimation method should not be used on diseased patient-specific aortas.

Thirdly, inner surface curvature magnitudes are significantly greater than centerline curvatures for diseased thoracic aortas which makes a crucial difference when describing boundary conditions for endografts, which are placed on the luminal aortic surfaces.

Fourthly, a predictive method relying on explicit inner longitudinal surface curvature and cross-sectional metrics was developed. This method can preoperatively give recommendations on optimal landing zones in order to avoid device malapposition.

Fifthly, the effects of TEVAR on multiaxial aortic motion have shown to be stiffening, *i.e.*, decreased longitudinal surface curvature deformation and cross-sectional deformation in the stented segment, which result in increased deformation for non-stented portions.

Sixthly, true lumen morphology for dissected thoracic aortas and helical metrics could be quantified. Initial studies show that luminal surfaces of thoracic aortas with type B dissection favors two modes of chirality as they propagate inside the whole aorta: they are either achiral and stay on the inner curve, or they are exclusively right-handed chiral and spirals clockwise distally.

Finally, TEVAR has shown to alter both helical and cross-sectional properties to, in most cases, a more favourable state for lower blood flow resistance. Subgroup analyses reveal that acute and chronic dissections were not improved to the same extent, and preoperative sub-grouping based on chirality vanished after TEVAR.

## 7 Discussion

Without going all the way back to Da Vinci’s remarkable insights on anatomy and physiology already during the 16<sup>th</sup> century or even further [58], let’s try to put our era of highly technically-oriented medicine, and the contents of this thesis, into perspective by glancing at some breakthroughs from the last century.

Since Röntgen’s first x-ray image in 1895 [59], imaging quality has improved exponentially with a growing number of modalities and unprecedented accuracy and patient safety. Halfway though these 120 years of improvements in imaging and radiology, the application to blood vessel imaging, angiography, started to become widely used thanks to Seldinger who outlined his *Seldinger technique* in 1953 [60].

In 1959 Nitinol was invented at the Naval Ordnance Laboratory but it would not be until 1986 this nickel-titanium alloy and its shape-preserving and superelastic properties was utilized successfully as a part of treating coronary artery disease when Wallstén’s self-expanding Wallstent<sup>®</sup> was implanted by percutaneous coronary intervention [61–63].

The boundaries were yet again to be pushed as pioneers like Volodos who described endovascular aortic repair in 1986, Parodi who used stent grafts to treat abdominal aortic aneurysm in 1990, and maybe more relevant in this thesis, when Dake placed an endograft to treat a descending thoracic aortic aneurysm in 1992 [25–27]. The devices used were modified stents where the graft material was added by the surgeons. These first *ad hoc* type endografts has then evolved and today there is a wide range of device types with most being intended for off-the-shelf use and in some cases with modifications or even being built customized for the patient-specific anatomy from the factory.

Geometric modeling can be the glue that allows for synergistic improvements of imaging, devices, and surgical techniques to allow for better procedural outcomes, and tying together these parts has never been more relevant, as technology is taking incrementally larger place in the vascular surgery speciality (and in medicine in general). The work presented in this thesis gives an example of how geometrical modeling can be used with the interdisciplinary collaboration at its core. The focus is on development of tools to allow for investigation of clinically relevant hypotheses. We show that automatic tools for cross-sectional slicing and quantification of surface metrics for single and dual lumina of thoracic aortas can be developed, validated, and applied in patient-specific cases. We perform and present studies to investigate geometric properties and morphology of diseased thoracic aortas, and how TEVAR changes these. The discovery of true lumen chiral bimodality, and how this phenomena is seen throughout nature reminds us that the human body is a biological system with a design intertwined with the very fabric of nature (see Figure 7.1 for a creative illustration giving a nod to this). Profound understanding of anatomy and pathology is fundamental in order to improve treatments. In this thesis, it is evaluated how TEVAR alters morphology relevant for the physiological function of the aorta. It is evident that TEVAR may not just have a local influence, but rather alters the dynamic conditions and the overall function for the whole thoracic aorta. The established geometric modeling methods form a good basis for further research studies based on observations in the clinic, this is further elaborated on in Section 8.

When the rapid development of artificial intelligence and machine learning ultimately arrives to a point where they surpass the accuracy of manual and semi-manual vessel

segmentation methods, the work presented in this thesis can come to good use. This since the outlined geometric modeling methodology accepts arbitrary surface input in the form of triangulated 3D surfaces (STL format) and is designed to be a wide foundation and ultimately bridging to the clinical setting. It is uncertain when we arrive to this point, but it is likely that it will bring a new paradigm in vessel segmentation. This may lead to breakthroughs that qualify for being mentioned in the context of the scientists, vascular surgeons, interventional radiologists, and engineers among who listed above. Every step, big and small, contributes to paving the way for the increasingly sophisticated treatments and endografts of tomorrow.

To conclude, the work summarized in this thesis contributes to the three aims of the project: 1) it has added knowledge about pathology and morphological implications on pathophysiology for dissections, 2) it has given insight valuable for clinicians in their treatment planning, 3) and it has provided medical device manufacturers with more nuanced boundary conditions to assist design improvements.

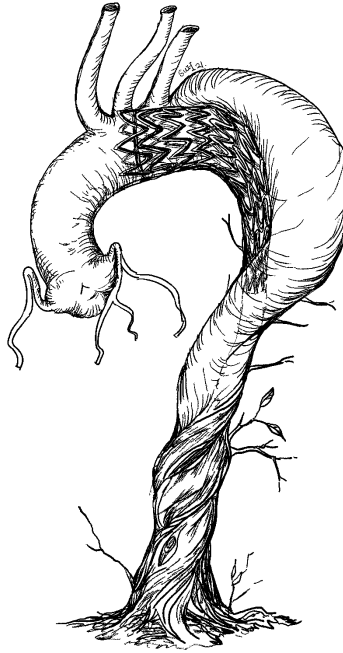


Figure 7.1: Illustration of a thoracic aorta after thoracic endovascular repair of a type B dissection including a distal portion inspired by the findings in **Paper D** and twinning tree trunks, like the ones Darwin observed [49].

## 8 Future Work

The work presented in appended **Papers A-E**, summarized in this thesis, has several natural continuations achieved by application of validated methodology for additional hypotheses and generalization to broaden the usability. With this said, the proposed future work is a moving target and especially the more clinically-oriented projects are subject to change. The future work can be categorized in three groups: 1) continuation, 2) helical morphology modeling, and 3) clinical implications/device related, as seen in Figure 8.1.

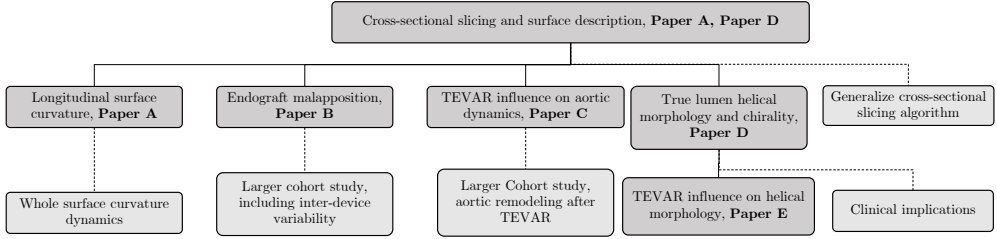


Figure 8.1: A schematic overview of the relationship between research in thesis (dark grey) and proposed future projects (light grey), *cf.* Figure 1.3.

In the *continuation* group we have the direct continuations and generalizations of the applications to **Papers A-C**. Building on **Paper A** a study of dynamic surface curvature for the whole surface could be conducted to complement the presented work in **Paper C**. With this, local curvature peaks can be evaluated and compared between pre- and post-TEVAR states. For **Paper B**, we envision future work by expanding the number of patients and investigating devices from different manufacturers, and also how *active control* delivery systems affect the bird-beaking issue. A proposed future work based solely on **Paper C** is to conduct a larger cohort study focusing on aortic remodeling after TEVAR, possibly even with monitored blood pressure to study hemodynamic effects.

In the *helical morphology modeling* group we have generalization of the cross-sectional slicing algorithm developed in **Paper A** and refined in **Paper D**. It would be possible to describe dual lumen pathology in the the ascending aorta (Type A dissections) and distal branch vessels, to arrive to a comprehensive model of true and false lumen interaction model involving the whole vasculature. Altogether, we have the following research questions related to helical modeling and dissection pathology:

- Would the helical angle of patients in a larger cohort of type B dissections also cluster into these two distinct groups (achiral and right-handed chiral)?
- Would type A dissections have a similar grouping of exclusively right-handed chiral or achiral propagation patterns as seen for type B aortic dissections?
- From a mechanistic standpoint; why do some dissections have a chiral propagation pattern, and some not?

Utilizing the full capabilities of the quantification toolbox developed and validated in this thesis, there are several possibilities for projects in the *clinical implications/device related* group. Complications due to excessive oversizing in dissection patients have recently been reported with examples such as retrograde type A dissections rising from the proximal landing zone and distal stent induced new entry (SINE) tears [64–66]. A SINE occurs when the radial force of the endograft at the distal end is so large that it protrudes the vessel wall creating a tear. Oversizing based on circumference could be preferred for thoracic cases (*cf.* abdominal cases in [40, 41]) resulting in etiology-specific recommendations to help reducing the risk for complications. Related to oversizing and configuration of endografts, a study on how the flow lumen is affected is also proposed. In some cases, multiple endografts are used in an overlapping configuration to create a longer endografted portion, but sometimes also to achieve a stepwise taper. This may be especially important in chronic dissections, where the vessel wall is less pliable and the true lumen is tapered [19, 20]. In the current project, cases with partially deployed endografts in overlapping configurations have been observed and these seem to cause local narrowing of the flow lumen as a consequence. As visualized in Figure 8.2B, it is seen that the shaded area between the abluminal (outer endograft surface) and luminal (inner endograft surface) surfaces is a volume obstructed by endograft material. This local narrowing creates a discontinuity of the flow lumen which can disturb the laminar blood flow and create recirculation zones, which are expected to increase risk for thrombus formation [67]. Additionally, these situations can also be of interest from a durability perspective as endografts cannot deploy fully (with high levels of measured oversizing post-TEVAR, as seen in Figure 8.2B) and potentially exhibit a higher mean stress than what they are designed for. This project will use the methods for pointwise surface tracking to determine the risks associated with different device configurations, types and sizes to, in the spirit of this thesis, aid clinicians in the treatment planning and provide insights valuable for further improvement of endovascular devices.

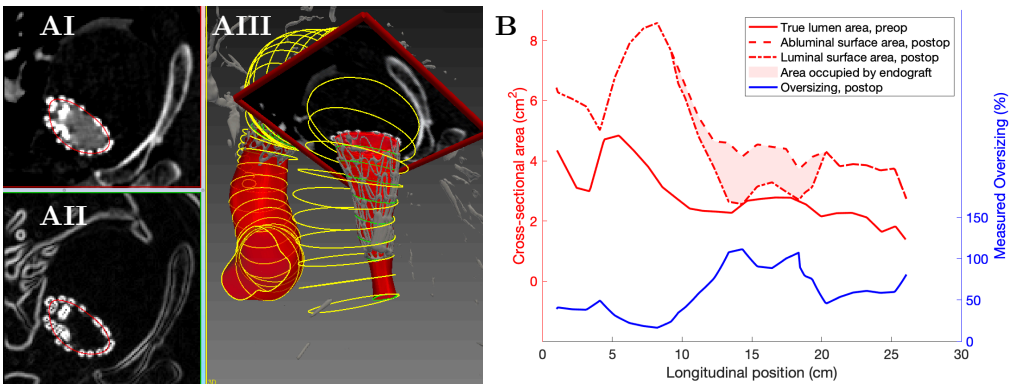


Figure 8.2: Figures AI and AII shows cross-sectional views, and AIII shows a 3D rendering of a cross-sectional contour in the distal end of the portion with overlapping endografts. Figure B shows cross-sectional area for the pre-TEVAR luminal surface as well as post-TEVAR luminal and abluminal surfaces and oversizing computed post-TEVAR.

# References

- [1] World Health Organization. *Cardiovascular Diseases (CVDs)*. 2017. URL: [https://www.who.int/news-room/fact-sheets/detail/cardiovascular-diseases-\(cvds\)](https://www.who.int/news-room/fact-sheets/detail/cardiovascular-diseases-(cvds)) (visited on 04/08/2021).
- [2] Takuya Ueda, Dominik Fleischmann, Michael D. Dake, Geoffrey D. Rubin, and Daniel Y. Sze. “Incomplete Endograft Apposition to the Aortic Arch: Bird-Beak Configuration Increases Risk of Endoleak Formation after Thoracic Endovascular Aortic Repair”. *Radiology* 255.2 (2010), pp. 645–652. DOI: <https://doi.org/10.1148/radiol.10091468>.
- [3] Yoshiaki Katada, Shunichi Kondo, Eitoshi Tsuboi, Ken Nakamura, Kyu Rokkaku, and Yoshihito Irie. “Type IA endoleak embolization after TEVAR via direct transthoracic puncture”. *Japanese Journal of Radiology* 33.3 (2015), pp. 169–172. DOI: [10.1007/s11604-015-0392-7](https://doi.org/10.1007/s11604-015-0392-7).
- [4] W Charles Sternbergh 3rd, Samuel R. Money, Roy K. Greenberg, Timothy A. M. Chuter, and Zenith Investigators. “Influence of Endograft Oversizing on Device Migration, Endoleak, Aneurysm Shrinkage, and Aortic Neck Dilation: Results From the Zenith Multicenter Trial”. *Journal of Vascular Surgery* 39.1 (2004), pp. 20–26. DOI: [10.1016/j.jvs.2003.09.022](https://doi.org/10.1016/j.jvs.2003.09.022).
- [5] Markus G.M. Steinbauer, Alexander Stehr, Karin Pfister, Thomas Herold, Niels Zorger, Ingolf Töpel, Christian Paetzel, and Piotr M. Kasprzak. “Endovascular repair of proximal endograft collapse after treatment for thoracic aortic disease”. *Journal of Vascular Surgery* 43.3 (2006), pp. 609–612. DOI: [10.1016/j.jvs.2005.11.045](https://doi.org/10.1016/j.jvs.2005.11.045).
- [6] Christopher P. Cheng. *Handbook of Vascular Motion*. 1st ed. Academic Press, an Elsevier imprint, 2019. ISBN: 978-0-12-815713-8.
- [7] C. Myers, B. Wolf, M. Nilson, A. Byrne, S. Rush, J. Elkins, A. Ragheb, B. Roeder, R. Swift, J. Metcalf, T. Duerig, and Christopher P. Cheng. “Handbook of Vascular Motion”. Ed. by Christopher P. Cheng. 1st ed. Academic Press, an Elsevier imprint, 2019. Chap. Product Development and Business Implications, pp. 351–372. ISBN: 978-0-12-815713-8.
- [8] Då.nu. *PET/CT-scanner på Karolinska universitetssjukhuset Huddinge*. Licensed with CC BY-SA 4.0. 2021. URL: [https://commons.wikimedia.org/wiki/File:PET\\_CT\\_scanner.JPG](https://commons.wikimedia.org/wiki/File:PET_CT_scanner.JPG) (visited on 02/10/2021).
- [9] Craig Bonsignore. *Open Stent Design*. Licensed with CC-BY-SA 3.0. Nitinol Devices & Components (NDC), <http://nitinol.com>. URL: <https://github.com/cbonsig/open-stent> (visited on 02/10/2021).
- [10] Gerald J. Tortora and Barry Derrickson. *Principles of Anatomy and Physiology*. 13th ed. Wiley, 2013. ISBN: ES8-1-118-34500-9.
- [11] John A. Elefteriades. “Natural History of Thoracic Aortic Aneurysms: Indications for Surgery, and Surgical Versus Nonsurgical Risks”. *The Annals of Thoracic Surgery* 74.5 (2002), pp. 1877–1880. DOI: [10.1016/s0003-4975\(02\)04147-4](https://doi.org/10.1016/s0003-4975(02)04147-4).
- [12] David S. Strayer and Emanuel Rubin. *Rubin’s Pathology. Clinicopathologic Foundations of Medicine*. 7th ed. LWW, 2014. ISBN: 978-1451183900.

- [13] CIRSE. *Thoracic endovascular aortic repair(TEVAR)*. 2020. URL: <https://www.cirse.org/patients/ir-procedures/thoracic-endovascular-aortic-repair-tevar/> (visited on 04/19/2021).
- [14] Sergio Ruiz de Galarreta, Aitor Cazón, Raúl Antón, and Ender A. Finol. “The Relationship Between Surface Curvature and Abdominal Aortic Aneurysm Wall Stress”. *European Journal of Cardio-Thoracic Surgery* 139.8 (2017), pp. 718–724. DOI: 10.1115/1.4036826.
- [15] T. Christian Gasser. “Biomechanical Rupture Risk Assessment: A Consistent and Objective Decision-Making Tool for Abdominal Aortic Aneurysm Patients”. *AORTA (Stamford)* 4.2 (2016), pp. 42–60. DOI: 10.12945/j.aorta.2015.15.030.
- [16] Judy Shum, Giampaolo Martufi, Elena Di Martino, Christopher B. Washington, Joseph Grisafi, Satish C. Muluk, and Ender A. Finol. “Quantitative Assessment of Abdominal Aortic Aneurysm Geometry”. *Annals of Biomedical Engineering* 39.1 (2011), pp. 277–286. DOI: 10.1007/s10439-012-0691-4.
- [17] E. Stanley Crawford. “The diagnosis and management of aortic dissection”. *Journal of the American Medical Association* 264.19 (1990), pp. 2537–2541. DOI: 10.1001/jama.1990.03450190069031.
- [18] Johnny Steuer, Martin Björck, Dieter Mayer, Anders Wanhainen, Thomas Pfammatter, and Mario Lachat. “Distinction between Acute and Chronic Type B Aortic Dissection: Is there a Sub-acute Phase?” *European Journal of Vascular and Endovascular Surgery* 45.6 (2013), pp. 627–631. DOI: 10.1016/j.ejvs.2013.03.013.
- [19] Xiaoying Lou, Edward P. Chen, Yazan M. Duwayri, Ravi K. Veeraswamy, William D. Jordan Jr, Carl A. Zehner, and Bradley G. Leshnower. “The impact of thoracic endovascular aortic repair on long-term survival in type B aortic dissection”. *Annals of Thoracic Surgery* 105.1 (2018), pp. 31–38. DOI: 10.1016/j.athoracsur.2017.06.016.
- [20] Ali Khoynezhad, Sherwin Toluie, and Talal Al-Atassi. “Treatment of the chronic type B aortic dissection: the pro-endovascular argument”. *Seminars in Thoracic and Cardiovascular Surgery* 29.2 (2017), pp. 131–136. DOI: 10.1053/j.semtcvs.2017.03.001.
- [21] Fabrizio Fanelli and Michael D. Dake. “Standard of Practice for the Endovascular Treatment of Thoracic Aortic Aneurysms and Type B Dissections”. *CardioVascular and Interventional Radiology* 32 (2009), pp. 849–860. DOI: 10.1007/s00270-009-9668-6.
- [22] Christoph A. Nienaber, Natzi Sakalihasan, Rachel E. Clough, Mohamed Aboukoura, Enrico Mancuso, James S. M. Yeh, Jean-Olivier Defraigne, Nick Cheshire, Ulrich Peter Rosendahl, Cesare Quarto, and John Pepper. “Thoracic endovascular aortic repair (TEVAR) in proximal (type A) aortic dissection: Ready for a broader application?” *The Journal of Thoracic and Cardiovascular Surgery* 153.3 (2018), pp. 3–22. DOI: 10.1016/j.jtcvs.2016.07.078.
- [23] Thomas Franz. *Cardiovascular and Cardiac Therapeutic Devices*. Springer, 2014. ISBN: 978-3-642-53836-0.
- [24] Thomas W. Duerig, Alan R. Pelton, and Dieter Stöckel. “An overview of nitinol medical applications”. *Materials Science and Engineering* 273-275 (1999), pp. 149–160. DOI: 10.1016/S0921-5093(99)00294-4.

- [25] Michael D. Dake, D. Craig Miller, Charles P. Semba, R. Scott Mitchell, Philip J. Walker, and Robert P. Liddell. “Transluminal Placement of Endovascular Stent-Grafts for the Treatment of Descending Thoracic Aortic Aneurysms”. *New England Journal of Medicine* 331.26 (1994), pp. 1729–1734. DOI: 10.1056/NEJM199412293312601.
- [26] Juan C. Parodi. “Endoluminal Treatment of Arterial Diseases Using a Stent-Graft Combination: Reflections 20 Years after the Initial Concept”. *Journal of Vascular Surgery* 37.4 (1997), pp. 3–4. DOI: 10.1177/152660289700400102.
- [27] Nikolay L. Volodos. “The 30th Anniversary of the First Clinical Application of Endovascular Stent-grafting”. *European Journal of Vascular and Endovascular Surgery* 49.5 (2015), pp. 495–497. DOI: 10.1016/j.ejvs.2015.02.012.
- [28] Donna D’Souza/Radiopaedia.com. *Eksempler på ”buksegraft” stenter som plasseres i bukens hovedpulsåre (aorta) og bekkenårer hvis de er utposet (aneurysme) eller svært trange*. Licensed with CC BY-NC-SA 3.0. URL: <https://sml.snl.no/stent> (visited on 02/10/2021).
- [29] Nathan Wilson, Kenneth Wang, Robert W. Dutton, and Charles Taylor. “A Software Framework for Creating Patient Specific Geometric Models From Medical Imaging Data for Simulation Based Medical Planning of Vascular Surgery”. *Medical Image Computing and Computer-Assisted Intervention, Lecture Notes in Computer Science* 2208 (2001). DOI: 10.1007/3-540-45468-3\_54.
- [30] Christopher P. Cheng, Yufei D. Zhu, and Ga-Young Suh. “Optimization of three-dimensional modeling for geometric precision and efficiency for healthy and diseased aortas”. *Computer Methods in Biomechanics and Biomedical Engineering* 21.1 (2018), pp. 65–74. DOI: 10.1080/10255842.2017.1423291.
- [31] Gilwoo Choi, Christopher P. Cheng, Nathan M. Wilson, and Charles A. Taylor. “Methods for quantifying three-dimensional deformation of arteries due to pulsatile and nonpulsatile forces: implications for the design of stents and stent grafts”. *Annals of Biomedical Engineering* 37.1 (2009), pp. 14–33. DOI: 10.1007/s10439-008-9590-0.
- [32] Albrecht Ludwig Friedrich Meister. “Generalia de genesi figurarum planarum, et independentibus earum affectionibus”. *Novi Commentarii Societatis Regiae Scientiarum Gottingensis* 1 (1769/79), 144–180 and plates 3-11.
- [33] Bahar Fata, Danielle Gottlieb, John E. Mayer, and Michael S. Sacks. “Estimated in Vivo Postnatal Surface Growth Patterns of the Ovine Main Pulmonary Artery and Ascending Aorta”. *Journal of Biomechanical Engineering* 135.7 (2013), pp. 71010–71012. DOI: 10.1115/1.4024619.
- [34] David B. Smith, Michael S. Sacks, David A. Vorp, and Michael Thornton. “Surface Geometric Analysis of Anatomic Structures Using Biquintic Finite Element Interpolation”. *Annals of Biomechanical Engineering* 28.6 (2000), pp. 598–611. DOI: 10.1114/1.1306342.
- [35] Torbjörn Lundh, Ga-Young Suh, Phillip DiGiacomo, and Christopher Cheng. “A Lagrangian cylindrical coordinate system for characterizing dynamic surface geometry of tubular anatomic structures”. *Medical and Biological Engineering and Computing* 56.9 (2018), pp. 1659–1668. DOI: 10.1007/s11517-018-1801-8.
- [36] Gilwoo Choi, Guanglei Xiong, Christopher P. Cheng, and Charles A. Taylor. “Methods for Characterizing Human Coronary Artery Deformation From Cardiac-Gated



- Computed Tomography Data”. *IEEE Transactions on Biomedical Engineering* 61.10 (2014), pp. 2582–2592. DOI: 10.1109/TBME.2014.2323333.
- [37] Giorgio Tomasi, Frans van den Berg, and Claus Andersson. “Correlation optimized warping and dynamic time warping as preprocessing methods for chromatographic data”. *Journal of Chemometrics* 18 (2004), pp. 231–241. DOI: 10.1002/cem.859.
- [38] Kongming Wang and Theo Gasser. “Alignment of curves by dynamic time warping”. *Annals of Statistics* 25.3 (1997), pp. 1251–1276. URL: <http://www.jstor.org/stable/2242521>.
- [39] Kibaek Lee, Junjun Zhu, Judy Shum, Yongjie Zhang, Satish C. Muluk, Ankur Chandra, Mark K. Eskandari, and Ender A. Finol. “Surface Curvature as a Classifier of Abdominal Aortic Aneurysms: A Comparative Analysis”. *Annals of Biomedical Engineering* 41.3 (2013), pp. 562–576. DOI: 10.1007/s10439-012-0691-4.
- [40] Ignance F.J. Tielliu, Ruben V.C. Buijs, Marcel Greuter, Tryfon Vainas, Bas M. Wallis de Vries, Ted R. Prins, and Clark J. Zeebregts. “Circumference as an alternative for diameter measurement in endovascular aneurysm repair”. *Medical Hypotheses* 85 (2015), pp. 230–233. DOI: 10.1016/j.mehy.2015.05.004.
- [41] Ruben V.C. Buijs, Clark J. Zeebregts, Tineke P. Willems, Tryfon Vainas, and Ignance F.J. Tielliu. “Endograft Sizing for Endovascular Aortic Repair and Incidence of Endoleak Type 1A”. *PloS ONE* 11.6 (2016). DOI: 10.1371/journal.pone.0158042.
- [42] Dassault Systemes Vélizy-Villacoublay France. *CATIA*. Version V5.
- [43] Christopher P. Cheng, Yufei D. Zhu, and Ga-Young Suh. “Optimization of three-dimensional modeling for geometric precision and efficiency for healthy and diseased aortas”. *Computer Methods in Biomechanics and Biomedical Engineering* 21.1 (2018), pp. 65–74. DOI: 10.1080/10255842.2017.1423291.
- [44] Joffrey van Prehn, Felix J.V. Schlösser, Bart E. Muhs, Hence J.M.Verhagen, Frans L. Moll, and Joost A. van Herwaarden. “Oversizing of Aortic Stent Grafts for Abdominal Aneurysm Repair: A Systematic Review of the Benefits and Risks”. *European Journal of Vascular and Endovascular Surgery* 38.1 (2009), pp. 42–53. DOI: 10.1016/j.ejvs.2009.03.025.
- [45] Tomoaki Kudo, Toru Kuratani, Kazuo Shimamura, Tomohiko Sakamoto, Keiwa Kin, Kenta Masada, Takayuki Shijo, Kei Torikai, Koichi Maeda, and Yoshiki Sawa. “Type 1a endoleak following Zine 1 and Zone 2 thoracic endovascular aortic repair: effect of bird-beak configuration”. *European Journal of Cardio-Thoracic Surgery* 52.4 (2017), pp. 718–724. DOI: 10.1093/ejcts/ezx254.
- [46] Frank J. Massey Jr. “The Kolmogorov-Smirnov Test for Goodness of Fit”. *American Statistical Association* 46.253 (1951), pp. 68–78. URL: <https://www.jstor.org/stable/2280095>.
- [47] Keith M. Ashman, Christina M. Bird, and Steven E. Zepf. “Detecting Bimodality in Astronomical Datasets”. *The Astronomical Journal* 108.6 (1994), pp. 2348–2361. DOI: 10.1086/117248.
- [48] Louis Pasteur. “Recherches sur les propriétés spécifiques des deux acides qui composent l’acide racémique”. *Annales de chimie et de physique* 28 (1850), pp. 56–99.
- [49] Charles Darwin. *The Movements and Habits of Climbing Plants*. John Murray, 1875.

- [50] James D. Watson and Francis H. C. Crick. “A structure for deoxyribose nucleic acid”. *Nature* 171 (1953), pp. 737–738.
- [51] T. Christian Gasser and Gerhard A. Holzapfel. “Modeling the Propagation of Arterial Dissection”. *European Journal of Mechanics A/Solids* 25.4 (2006), pp. 617–633. DOI: 10.1016/j.euromechsol.2006.05.004.
- [52] Osman Gültekin, Sandra P. Hager, Hüsni Dal, and Gerhard A. Holzapfel. “Computational modeling of progressive damage and rupture in fibrous biological tissues: application to aortic dissection”. *Biomechanics and Modeling in Mechanobiology* 18.6 (2019), pp. 1607–1628. DOI: 10.1007/s10237-019-01164-y.
- [53] Allen Cheng, Paul Dagum, and D. Craig Miller. “Aortic Root Dynamics and Surgery: From Craft to Science”. *Philosophical transactions of the Royal Society of London. Series B, Biological sciences* 362.1484 (2007), pp. 1407–1419. DOI: 10.1098/rstb.2007.2124.
- [54] Kwong M. Tse, Peixuan Chiu, Heow P. Lee, and Pei Ho. “Investigation of hemodynamics in the development of dissecting aneurysm within patient-specific dissecting aneurismal aortas using computational fluid dynamics (CFD) simulations”. *Journal of Biomechanics* 44.5 (2011), pp. 827–836. DOI: 10.1016/j.jbiomech.2010.12.014.
- [55] Zhang Jinsou and Zhang Benzhaoh. “Fluid flow in helical pipe”. *Acta Mechanica Sinica* 15.4 (1999), pp. 299–312. DOI: 10.1007/BF02487928.
- [56] John Lekner. “Viscous flow through pipes of various cross-sections”. *European Journal of Physics* 28.3 (2007), pp. 521–527. DOI: 10.1088/0143-0807/28/3/014.
- [57] John E. Hall. *Guyton and Hall Textbook of Medical Physiology*. 13th ed. Elsevier, 2016. ISBN: 978-1-4557-7016-8.
- [58] John B. West. “Leonardo da Vinci: engineer, bioengineer, anatomist, and artist”. *American Journal of Physiology - Lung Cellular and Molecular Physiology* 312.3 (2017), pp. L392–L397. DOI: 10.1152/ajplung.00378.2016.
- [59] Wilhelm C. Röntgen. “Über eine neue Art von Strahlen”. *Sitzungsberichte Der Physikalisch-Medizinischen Gesellschaft zu Würzburg* (1895).
- [60] Sven Ivar Seldinger. “Catheter replacement of the needle in percutaneous arteriography: A new technique”. *Acta Radiologica* 39.5 (1953), pp. 368–376. DOI: 10.3109/00016925309136722.
- [61] Ulrich Sigwart, Jacques Puel, Velimir Mirkovitch, Francis Joffre, and Lukas Kappenberg. “Intravascular stents to prevent occlusion and restenosis after transluminal angioplasty”. *The New England journal of medicine* 316.12 (1987), pp. 701–706. DOI: 10.1056/NEJM198703193161201.
- [62] William J. Buehler, John V. Gilfrich, and R. C. Wiley. “Effect of Low-Temperature Phase Changes on the Mechanical Properties of Alloys near Composition TiNi”. *Journal of Applied Physics* 34.5 (1963), pp. 1475–1477. DOI: 10.1063/1.1729603.
- [63] Frederick E. Wang, William J. Buehler, and Stanley J. Pickart. “Crystal Structure and a Unique ”Martensitic” Transition of TiNi”. *Journal of Applied Physics* 36.10 (1965), pp. 3232–3239. DOI: 10.1063/1.1702955.
- [64] Lei Liu, Simeng Zhang, Qingsheng Lu, Zaiping Jing, Suming Zhang, and Bing Xu. “Impact of oversizing on the risk of retrograde dissection after TEVAR for acute and chronic type B dissection”. *Journal of Endovascular Therapy* 23.4 (2016), pp. 620–625. DOI: 10.1177/1526602816647939.

- [65] Hyunsik Jang, Man-Deuk Kim, Gyoung M. Kim, Jong Y. Won, Young-Guk Ko, Donghoon Choi, Hyun-Chul Joo, and Do Y. Lee. “Risk factors for stent graft-induced new entry after thoracic endovascular aortic repair for Stanford type B dissection”. *Journal of Vascular Surgery* 65.3 (2017), pp. 676–685. DOI: 10.1016/j.jvs.2016.09.022.
- [66] Ludovic Canaud, Baris A. Ozdemir, Benjamin O. Patterson, Peter J. E. Holt, Ian M. Loftus, and Matt M. Thompson. “Retrograde aortic dissection after thoracic endovascular aortic repair”. *Annals of Surgery* 260.2 (2014), pp. 389–395. DOI: 10.1097/SLA.0000000000000585.
- [67] James J Hathcock. “Flow effects on coagulation and thrombosis”. *Arteriosclerosis, thrombosis, and vascular biology* 26.8 (2006), pp. 1729–1737. DOI: 10.1161/01.ATV.0000229658.76797.30.

